

Collision dynamics at medium and relativistic energies

M. Colonna¹

¹INFN, Laboratori Nazionali del Sud, I-95123 Catania, Italy

March 6, 2020

Abstract

Recent results connected to nuclear collision dynamics, from low up to relativistic energies, are reviewed. Heavy ion reactions offer the unique opportunity to probe the complex nuclear many-body dynamics and to explore, in laboratory experiments, transient states of nuclear matter under several conditions of density, temperature and charge asymmetry. From the theoretical point of view, transport models are an essential tool to undertake these investigations and make a connection between the nuclear effective interaction and sensitive observables of experimental interest. In this article, we mainly focus on the description of results of transport models for a selection of reaction mechanisms, also considering comparisons of predictions of different approaches. This analysis can help understanding the impact of the interplay between mean-field and correlation effects, as well as of in-medium effects, on reaction observables, which is an essential point also for extracting information on the nuclear Equation of State. A special emphasis will be given to the review of recent studies aimed at constraining the density behavior of the nuclear symmetry energy. For reactions at medium (Fermi) energies, we will describe light particle and fragment emission mechanisms, together with isospin transport effects. Collective effects characterizing nuclear collision dynamics, such as transverse and elliptic flows, will be discussed for relativistic heavy ion reactions, together with meson production and isotopic ratios.

Contents

1	Introduction	2
2	Theoretical description of collision dynamics	5
2.1	Semi-classical approximation and BUU models	6
2.2	Semi-classical stochastic models	7
2.3	Fluctuations in full phase space and the BLOB model	8
2.4	Fluctuation projection and simplified stochastic approaches	9
2.5	QMD models	10
2.6	Antisymmetrized Molecular Dynamics	11
2.7	Relativistic transport approaches	12
2.7.1	QHD effective field theory	12
2.7.2	Relativistic semi-classical transport equations	13
3	Effective interactions and symmetry energy	14

4	Reaction dynamics at medium energy: central collisions	17
4.1	Pre-equilibrium nucleon and cluster emission	18
4.1.1	Isospin effects	18
4.2	Multifragment emission	20
4.2.1	Isotopic features	23
4.3	Concluding remarks on multifragmentation	25
5	Reaction dynamics at medium energy: semi-peripheral collisions	26
5.1	Isospin transport at Fermi energies	27
5.1.1	Charge equilibration in peripheral collision dynamics	29
5.1.2	Neck fragmentation at Fermi energies: isospin dynamics	31
5.2	Comparison between the predictions of different transport models	34
6	Collision dynamics at relativistic energies	36
6.1	Collective flows and isospin effects	38
6.2	Meson production	40
7	Conclusions and perspectives	44
8	Acknowledgements	46

1 Introduction

Many experimental and theoretical efforts have been devoted, over the past 40 years or so, to the study of nuclear reactions from low to relativistic energies, to probe new aspects of collision dynamics and scrutinize relevant properties of the nuclear medium. Indeed, heavy ion collision experiments, where transient states of nuclear matter (NM), spanning a wide spectrum of regimes, are created, provide crucial insights into the features of the nuclear Equation of State (EOS). The latter is a rather important object, which influences a large variety of phenomena, ranging from the structure of nuclei and their decay modes, up to the life and the properties of massive stars. In particular, the understanding of the properties of exotic nuclei, as well as neutron stars and supernova dynamics, entails the knowledge of the behavior of nuclear symmetry energy.

Measurements of experimental observables linked to isoscalar collective vibrations in nuclei, collective flows and meson production in nuclear reactions, have contributed to constrain the EOS of charge symmetric matter for densities up to five times the saturation value [1]. More recently, the availability of exotic beams has made it possible to explore, in laboratory conditions, new aspects of nuclear structure and dynamics up to extreme ratios of neutron (N) to proton (Z) numbers, thus giving a strong boost to the investigation of the EOS of asymmetric matter.

The low-density regime has an impact on reaction dynamics at Fermi energy (isotopic features in fragmentation [2], charge equilibration [3, 4]), as well as on nuclear structure (neutron skins, pygmy resonances [5]) and in the astrophysical context (neutron star formation and crust [6, 7, 8]). On the other hand, relativistic heavy ion reactions (isospin flows, meson production [9, 10]) and compact star features (neutron star mass-radius relation, cooling, hybrid structure, formation of black holes [6, 11]) are strongly influenced by the high density behavior of the symmetry energy.

In this article, we will discuss heavy ion reactions in the beam energy domain mentioned above, ranging from few tens of MeV/nucleon (Fermi energy domain) up to several hundred MeV/nucleon (relativistic energy regime). The overall reaction dynamics appears characterized by an initial compression phase, where, depending on beam energy and reaction centrality, densities up to two-three

times the saturation density can be reached. A significant degree of thermalization, together with “pre-equilibrium” light particle emission, is expected, especially in central reactions. During the following expansion phase (on characteristic time scales of the order of 10-100 fm/c), several clusters and nuclear fragments are produced from a hot source whose excitation energy is typically comparable to the binding energy (per nucleon) of a nucleus [12, 13, 14]. One also observes the development of collective flows, such as radial flow of the initially compressed matter and/or transverse flow of the spectator matter.

From the theoretical point of view, understanding the features and the reaction mechanisms involving complex systems, such as nuclei, in terms of their constituent particles and the interaction among them is a true challenge. The original quantal many-body problem, is often approached adopting the mean-field approximation (or suitable extensions), yielding a so-called effective interaction [15, 16, 17, 18]. Hence, one can say that the collision dynamics is governed to a large extent by the details of the nuclear effective interaction, which provides the nuclear EOS in the equilibrium limit. However, many-body correlations, beyond the mean-field picture, are important and certainly influence the disassembly of the composite nuclear system and its re-aggregation in new configurations along the reaction path. In general, it is more appropriate to state that the reaction dynamics is ruled by the delicate interplay between mean-field effects and many-body correlations. Hence the investigation of heavy ion reactions presents a twofold interest: to unveil new aspects of the complex nuclear dynamics and, at the same time, to probe relevant features of the nuclear effective interaction and EOS. It is clear that the two goals are intertwined: the extraction of robust constraints on the EOS relies on suitable descriptions of the reaction dynamics.

Several extensions of mean-field models have to be introduced to take explicitly into account the effects of relevant interparticle correlations. Focusing on nuclear dynamics, an intense theoretical work on correlations and density fluctuations has started in the past years, fostered by the availability of large amounts of experimental data on fragment formation and light cluster production in intermediate energy heavy ion collisions [19, 20, 21, 22, 23, 24], also in connection with the possibility to observe volume (spinodal) instabilities and liquid-gas phase transitions in nuclei. In passing, we note that low-density clustering is of interest also in other contexts where nuclear matter at subsaturation densities can appear, such as the conditions encountered in the crust of neutron stars and/or along supernova explosion processes [6]. Sophisticated thermodynamical approaches have been formulated to evaluate the EOS of clustered matter, which can be employed in astrophysical applications [25]. For instance, the appearance of clusters is expected to influence neutrino transport, thus modifying the cooling mechanism by neutrino emission of protoneutron stars [26, 27, 28].

A commonly employed scheme to deal with the dynamics of nuclear collisions at intermediate energy is represented by semi-classical transport theories, such as the Nordheim approach, in which the Vlasov equation for the one-body phase space density, $f(\mathbf{r}, \mathbf{p}, t)$, is extended by the introduction of a Pauli-blocked Boltzmann collision term [29, 30], which accounts for the average effect of the two-body residual interaction. Thus the resulting transport equation, often called Boltzmann-Uehling-Uhlenbeck (BUU) equation, contains two basic ingredients: the self-consistent mean-field potential and the two-body scattering cross sections. In order to introduce fluctuations and further (many-body) correlations in transport theories, a number of different avenues have been taken, that can be essentially reconducted to two different classes of models (see Ref.[31] for a recent review). One is the class of molecular dynamics (MD) models [24, 32, 33, 34, 36, 35, 37, 38] while the other kind is represented by stochastic mean-field approaches [39, 40, 41, 23]. In the latter approaches, fluctuations of the one-particle density, which should account for the effect of the neglected many-body correlations, are introduced by adding to the transport equation a stochastic term, representing the fluctuating part of the collision integral [39, 40, 41], in close analogy with the Langevin equation for a Brownian motion. This extension leads to the Boltzmann-Langevin (BL) equation, which can be derived as the next-order correction, in the equation describing the time evolution of f , with respect to the standard average collision integral. Within such a description, though the system is still described solely in terms of the reduced one-body

density f , this function may experience a stochastic time evolution in response to the random effect of the fluctuating collision term. The effects of the fluctuations introduced are particularly important when instabilities or bifurcations occur in the dynamics. Indeed this procedure is suitable for addressing multifragmentation phenomena where clusters emerge from the growth of density inhomogeneities, driven by the unstable mean-field. However, the fluctuations introduced in this way are not strong enough to fully account for the production of light clusters, which are loosely bound by the mean-field and would require stronger nucleon correlations.

In molecular dynamics models the many-body state is represented by a simple product wave function, with or without antisymmetrization. The single particle wave functions are usually assumed to have a fixed Gaussian shape. In this way, though nucleon wave functions are supposed to be independent (mean-field approximation), the use of localised wave packets induces many-body correlations both in mean-field propagation and hard two body scattering (collision integral), which is treated stochastically. Hence this way to introduce many-body correlations and produce a possible trajectory branching is essentially based on the use of localized nucleon wave packets.

These approaches (in particular, the AMD approach [24]) have shown to be quite successful in describing the clustered structures characterising the ground state of several light nuclei [42]. Moreover, as far as nuclear dynamics is concerned, the wave function localisation appears quite appropriate to describe final fragmentation channels, where each single particle wave function should be localised within a fragment. However, one should notice that the use of fixed shape localised wave packets in the full dynamics could affect the correct description of one-body effects, such as spinodal instabilities and zero sound propagation [34, 43]. A simplistic description of the differences between the two classes of models would be to say that (extended) mean-field models may lack many-body correlations, whereas molecular dynamics models are mainly classical models.

The approaches discussed so far are mostly based on non-relativistic formalisms, in which non-nucleonic degrees of freedom are integrated out giving nucleon-nucleon potentials. Then nuclear matter is described as a collection of quantum non-relativistic nucleons interacting through an instantaneous effective potential. This prescription is mainly employed in the medium-energy collisional domain.

On the other hand, reactions at relativistic energies are more properly described via a fully covariant transport approach, related to an effective field exchange model, where the relevant degrees of freedom of the nuclear dynamics are accounted for [44, 45]. This leads to a propagation of particles (nucleons and mesons) suitably dressed by self-energies that will influence particle emission, collective flows and in medium nucleon-nucleon inelastic cross sections.

One of the goals of this review is to try to get a deeper insight into the interplay between mean-field effects and many-body correlations in light particle and fragment emission mechanisms, as well as on collective dynamics. A crucial point to be understood would be the extent of the impact of many-body correlations on the global reaction dynamics (such as compression-expansion, development of collective flows, thermalization, charge equilibration) and on corresponding reaction observables which are expected to reflect specific ingredients of the nuclear effective interaction. Sizeable effects could be expected on the basis of the different energetics and of the reduction of the degrees of freedom induced by the formation of clusters and fragments.

For reactions at relativistic energies, an important aspect to be discussed will be the impact of (isospin-dependent) in-medium effects, such as the modification of particle self-energies, on nucleon and meson emission.

We will review a selection of recent results on dissipative collisions in a wide range of beam energies, from reactions at Fermi energies up to the $AGeV$ range. Several observables, which are sensitive in particular to the isovector sector of the nuclear effective interaction and corresponding EOS terms (asyEOS) have been suggested [46, 47, 48, 8]. Fermi energies bring information on the EOS features (and symmetry energy term) around or below normal density, whereas intermediate energies probe higher density regions. We mainly focus on the description of results of transport models, trying to

compare predictions of different models and to probe the impact of the interplay between mean-field and correlation effects, as well as of in-medium effects, on reaction observables. This discussion will be framed also in the context of the present theoretical and experimental efforts aimed at constraining the density behavior of the symmetry energy.

The article is organized as it follows: A brief description of the transport models commonly employed in the treatment of collision dynamics at medium and relativistic energies is given in Section 2. Section 3 is devoted to the description of effective interactions used in transport models. A survey of results relative to the Fermi energy domain for central and semi-peripheral collisions is given in Sections 4 and 5, respectively. Section 6 is devoted to results of collision dynamics at relativistic energies. Finally conclusions and perspectives are drawn in Section 7.

2 Theoretical description of collision dynamics

Heavy ion collisions are rather intricate processes whose understanding would imply to solve the complex many-body problem. In principle, this task should be tackled by solving the many-body Schrödinger equation, to obtain the many-body state $|\Psi(t)\rangle$ at a time t . However, this is presently unaffordable in the general case; an important simplification derives from the fact that, for several practical purposes, it is enough to know, with sufficient accuracy, the corresponding solution for the system one-body density, thus reducing the problem to single-particle dynamics.

The one-body density operator $\hat{\rho}$ for a system containing A particles is defined as

$$\hat{\rho} = A \text{Tr}_{2,3,\dots,A} |\Psi\rangle\langle\Psi| \quad (1)$$

(The state $|\Psi\rangle$ is assumed to be normalized). From the knowledge of the one-body density operator $\hat{\rho}(t)$, it becomes possible to evaluate the expectation value of any one-body observable, thus allowing one to make predictions also for observables of experimental interest, in view of a comparison to data.

In presence of only two-body interactions $\sum_{i<j} v_{ij}$, one can deduce, for the time derivative of the one-body density $\frac{d}{dt}\hat{\rho}$, the following equation:

$$i\hbar \frac{\partial}{\partial t} \hat{\rho} = \left[\frac{1}{2m} \mathbf{p}^2, \hat{\rho} \right] + \text{Tr}_2 [v, \hat{\rho}^{(2)}], \quad (2)$$

where m is the particle mass and the two-body density operator $\hat{\rho}^{(2)}$, defined as

$$\hat{\rho}^{(2)} = A(A-1) \text{Tr}_{3,\dots,A} |\Psi\rangle\langle\Psi|, \quad (3)$$

has been introduced. The equation above shows that the knowledge of the two-body density operator is required to solve the exact time evolution of the one-body density. In turn, deriving the equation for the time evolution of the two-body density, one would see that it contains the three-body density operator, and so on. This actually corresponds to the Martin-Schwinger hierarchy set of equations (see e.g. Ref. [49]). In order to get a closed equation for the time evolution of $\hat{\rho}(t)$, it is necessary to resort to some kind of approximation, i.e. to truncate the hierarchy at a given level.

The simplest approximation corresponds to the independent particle picture, according to which the two-body density operator can be written as an anti-symmetrized product of one-body densities:

$$\hat{\rho}_{12}^{(2)} = \hat{A}_{12} \hat{\rho}_1 \hat{\rho}_2, \quad (4)$$

where \hat{A}_{12} is the antisymmetrization operator acting on a two-body state.

Then Eq. (2) can be reformulated as:

$$i\hbar \frac{\partial}{\partial t} \hat{\rho} = \left[\frac{1}{2m} \mathbf{p}^2 + U[\hat{\rho}], \hat{\rho} \right] \equiv \left[H_0[\hat{\rho}], \hat{\rho} \right], \quad (5)$$

where the mean-field potential $U[\hat{\rho}]$ has been introduced, that is defined as

$$U_1[\hat{\rho}] = \text{Tr} \hat{A}_{12} \nu_{12} \hat{\rho}_2. \quad (6)$$

A particular case, within the independent particle picture, would be to consider a Slater determinant for the many-body state $|\Psi\rangle$. This approximation corresponds to the time-dependent Hartree Fock (TDHF) approach. In practical applications, effective interactions are used for the mean-field potential, to account for the neglected correlations beyond the mean-field picture.

Extensions towards the inclusion of two-body correlations can be developed by including a correlated part in the two-body density operator, i.e.

$$\hat{\rho}_{12}^{(2)} = \hat{A}_{12} \hat{\rho}_1 \hat{\rho}_2 + \hat{\sigma}_{12}, \quad (7)$$

where the quantity $\hat{\sigma}_{12}$ encloses the explicit two-body correlation effects. Accordingly, the system Hamiltonian can be written as the sum of the term treated and the one-body level (H_0) and a residual two-body interactions: $H = H_0 + \nu_{12}$. Then neglecting three-body correlations and retaining only terms up to leading order in the residual interaction and/or the explicit two-body correlations, Eq.(5) will be extended as it follows:

$$i\hbar \frac{\partial}{\partial t} \hat{\rho} = [H_0[\hat{\rho}], \hat{\rho}] + K[\hat{\rho}, \nu_{12}] + \delta K[\nu_{12}, \hat{\sigma}_{12}] \quad (8)$$

The second term of the (r.h.s.) of Eq.(8) represents the average effect of the residual interaction, i.e. of the interaction which is not accounted for by the mean-field description, whereas the third term contains the explicit correlations $\hat{\sigma}_{12}$. In other words, the K term accounts for explicit two-body interactions, whereas the fluctuating term δK may even account for higher order correlations.

Fluctuations with respect to the mean-field trajectory might originate from the initial conditions, as well as from the dynamical evolution. We will come back to this point in deeper detail later, when we will discuss the semi-classical approximation. It may be noted that the equation above is similar to Stochastic TDHF (STDHF) [50], and it transforms into the extended TDHF (ETDHF) theory [51, 52, 53] if the fluctuating term δK is suppressed; ETDHF can in fact efficiently describe the behavior of some observables related to dissipative processes, but it can not follow possible bifurcation paths deviating from the mean trajectory.

New stochastic extensions have been recently proposed for time-dependent quantum approaches [54, 55]. A possibility is to inject quantum and/or thermal fluctuations just in the initial conditions of TDHF calculations, leading to a spread of dynamical trajectories and corresponding variances of physical observables. Interesting results have been obtained for the description of the spontaneous fission of superheavy systems [56].

2.1 Semi-classical approximation and BUU models

For the description of heavy ion reaction dynamics in the Fermi and intermediate energy regimes, Eq.(8) is often solved in the semi-classical approximation. Within such a scheme, the goal is to derive an equation for the time evolution of the one-body distribution function in phase space, $f(\mathbf{r}, \mathbf{p}, t)$, which is nothing but the semi-classical analog of the Wigner transform of the one body density matrix. The Boltzmann-Uehling-Uhlenbeck (BUU) theory can be considered as the semi-classical analog of Eq.(8), where the δK term is neglected. The BUU equation can also be directly derived from the Born-Bogoliubov-Green-Kirkwood-Yvon (BBGKY) hierarchy or, within the real-time Green's-function formalism, from the Kadanoff-Baym equations [57, 58, 59].

Considering, for the sake of simplicity, a mean-field potential depending only on the local density $\rho(\mathbf{r})$, in non-relativistic kinematics, the BUU equation reads:

$$\frac{\partial f(\mathbf{r}, \mathbf{p}, t)}{\partial t} + \frac{\mathbf{p}}{m} \cdot \frac{\partial f}{\partial \mathbf{r}} - \frac{\partial U[\rho]}{\partial \mathbf{r}} \cdot \frac{\partial f}{\partial \mathbf{p}} = \bar{I}_{coll}[f] \quad (9)$$

where the collision term \bar{I}_{coll} has been introduced, which represents the semi-classical analog of the K term on the r.h.s. of Eq.(8). The latter is written as:

$$\bar{I}_{coll}[f](\mathbf{r}, \mathbf{p}) = g \int \frac{d\mathbf{p}_1}{(2\pi\hbar)^3} d\Omega v_{rel} \frac{d\sigma}{d\Omega} [f' f'_1 (1-f)(1-f_1) - f f_1 (1-f')(1-f'_1)], \quad (10)$$

where g is the degeneracy factor and the coordinates of isospin are not shown for brevity.

The distribution function entering the above integral is evaluated at the coordinate \mathbf{r} and at four locations in momentum space, with the final momenta \mathbf{p}' and \mathbf{p}'_1 connected to the momenta \mathbf{p} and \mathbf{p}_1 by the scattering angle Ω and the energy and momentum conservation. Thus, within a classical picture, the effect of the two-body residual interaction is interpreted in terms of hard two-body scattering between nucleons. In Eq.(10), the quantity v_{rel} denotes the relative velocity between the two initial phase-space portions and $d\sigma/d\Omega$ represents the differential nucleon-nucleon (n-n) cross section, accounting for the residual interaction. In simulations of heavy ion collisions at intermediate energy, a density dependent screened value of the n-n cross section, accounting for in-medium effects, is often adopted (see, for instance, Refs.[60, 61]). The fermionic nature of the system is preserved by the Pauli-blocking factors (the terms like $(1-f)$).

Transport equations are usually solved numerically, adopting the test particle method [62], i.e. the system is sampled by N_{test} test-particle per nucleon.

2.2 Semi-classical stochastic models

As anticipated above, if a suited stochastic approach is adopted, simplified higher-order contributions to the dynamics are taken into account even though not explicitly implemented. Already within a first-order-truncation scheme, it was found that a stochastic approach, including fluctuations only in the initial conditions, can be used to restore all the BBGKY missing orders approximately [54], and generate large-amplitude fluctuations; in this case, a coherent ensemble of mean-field states is propagated along different trajectories from an initial stochastic distribution. Such scheme, which appears appropriate in low-energy framework, is however insufficient to address highly dissipative regimes. We will discuss in the following some approaches which attempt to solve Eq.(8), but within the semi-classical approximation. Thus we introduce the so-called Boltzman-Langevin equation (BLE) [40, 23]:

$$\frac{df}{dt} = \frac{\partial f}{\partial t} + \{f, H\} = \bar{I}_{coll}[f] + \delta I[f]. \quad (11)$$

Initial quantum fluctuations are neglected in this case and the stochastic treatment, mainly associated with hard two-body scattering, acts intermittently all along the temporal evolution, producing successive splits of a given mean-field trajectory into subensembles, as illustrated in Fig.(1). Within this framework, the system is still described in terms of the one-body distribution function f , but this function may experience a stochastic evolution in response to the action of the fluctuating term. When instabilities are encountered along the reaction path, the evolution of the fluctuation "seeds" introduced by the BL approach is then driven by the dissipative dynamics of the BUU evolution, allowing the system to choose its trajectory through possible bifurcations leading to different fragmentation paths. In this way a series of "events" are created in a heavy-ion collision, which can then be analyzed and sampled in various ways.

Assuming that fluctuations are of statistical nature, the term δI is simply interpreted as the fluctuating part of the collision integral, with a vanishing mean value and a variance which equals the average collision integral.

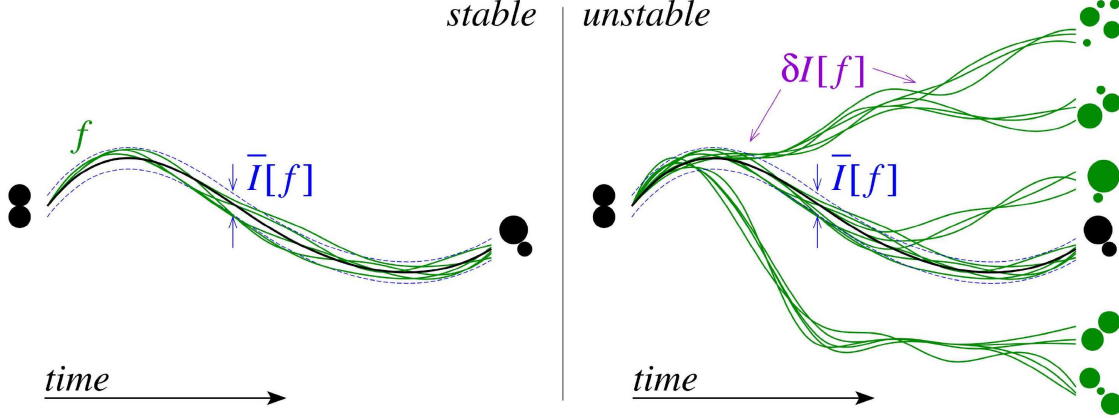


Figure 1: Illustration of the effect of fluctuations on a dynamical trajectory. In stable conditions a moderate spread of trajectories, around the average (associated with the average collision term $\bar{I}_{coll}[f]$) is observed (left panel). The right panel shows that in presence of instabilities the fluctuating BL term leads to bifurcation of trajectories. Taken from [63].

2.3 Fluctuations in full phase space and the BLOB model

The latter procedure can be implemented by replacing the residual terms ($\bar{I}_{coll} + \delta I$) by a similar Uehling Uhlenbeck (UU) - like term, involving nucleon packets, which respects the Fermi statistics both for the occupancy mean value and for the occupancy variance.

Thus one may consider a rescaled UU collision term where a single binary collision involves extended phase-space portions of nucleon distribution of the same type (neutrons or protons), A, B , to simulate nucleon wave packets, and Pauli-blocking factors act on the corresponding final states C, D , also treated as extended phase-space portions. The choice of defining each phase-space portion A, B, C and D so that the isospin number is either 1 or -1 is necessary to preserve the Fermi statistics for both neutrons and protons, and it imposes that blocking factors are defined accordingly in phase-space cells for the given isospin species. The above prescriptions lead to the Boltzmann Langevin One Body (BLOB) equations [64]:

$$\begin{aligned} \frac{\partial f}{\partial t} + \{f, H\} &= \bar{I}_{coll} + \delta I = \\ &= g \int \frac{d\mathbf{p}_b}{h^3} \int W(AB \leftrightarrow CD) F(AB \rightarrow CD) d\Omega. \end{aligned} \quad (12)$$

In the above equation, W is the transition rate, in terms of relative velocity between the two colliding phase-space portions and differential nucleon-nucleon cross section:

$$W(AB \leftrightarrow CD) = |v_A - v_B| \frac{d\sigma}{d\Omega}. \quad (13)$$

The term F contains the products of occupancies and vacancies of initial and final states over their full phase-space extensions:

$$F(AB \rightarrow CD) = \left[(1-f_A)(1-f_B)f_C f_D - f_A f_B (1-f_C)(1-f_D) \right]. \quad (14)$$

In practice, if the test-particle method is employed, the phase-space portions A, B, C and D should be agglomerates of N_{test} test-particles each, and the nucleon-nucleon cross section used in Eq. (13)

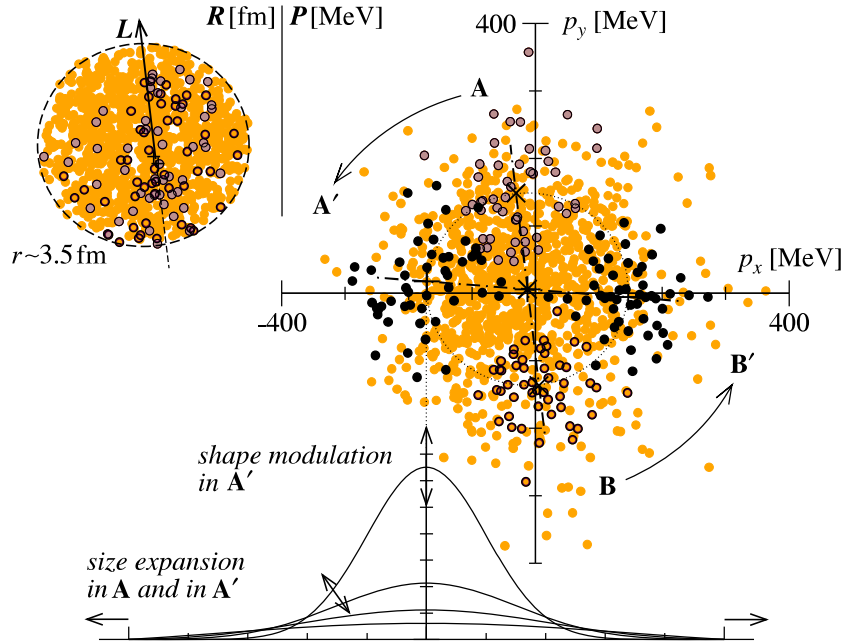


Figure 2: Example of one collision event in BLOB. Two nucleons are represented by two agglomerates of test particles A and B (black points) which share the same volume in coordinate space R . In the momentum space P the collision process induces a rotation, according to a given set of scattering angles (θ, ϕ) , to the destination sites A' and B', where the test particles are distributed according to Pauli-blocking and energy conservation constraints. The latter are enforced by modulating the shape and the size of the nucleon packet (see the bottom part of the figure). Taken from [67].

should be scaled by the same amount N_{test} , considering that each nucleon packet is associated with N_{test} possible samplings.

By this procedure, it can be shown that for a free Fermi gas, the occupancy variance at equilibrium equals $\bar{f}(1-\bar{f})$ in a phase-space cell h^3 , resulting from the movement of extended portions of phase space which have the size of a nucleon. Thus the residual term carries nucleon-nucleon correlations which fulfill the analytical predictions of an equilibrated fermionic system [65]. Hence, the BLOB approach exploits the stochastic term of Eq. (12), recovering correlation orders higher than the second order truncation (which would correspond to the average collision integral), and inducing the BL fluctuation-bifurcation scheme. The method is schematically illustrated in Fig.2.

A new framework to treat the dissipation and fluctuation dynamics associated with n-n scattering in heavy-ion collisions has been recently introduced in [66]. Two-body collisions are effectively described in terms of the diffusion of nucleons in the viscous nuclear medium, according to a set of Langevin equations in momentum space. The new framework, combined with the usual mean-field dynamics, has been shown to be suited to simulate heavy-ion collisions at intermediate energies. Applications of the method, as well as the comparison with other transport models, are presently in progress.

2.4 Fluctuation projection and simplified stochastic approaches

Several approximate treatments of the BL approach have been introduced and are still employed to deal with the description of collision dynamics. For instance, at variance with the above description, the stochastic term in the r.h.s. of Eq.(11) can be kept separate and treated as a stochastic force related to an external potential U' [68]. More generally, approximated stochastic mean-field approaches build fluctuations from suitable projections [69, 70] or introducing a well adapted external force or a distribution of initial conditions which should be accurately prepared in advance [23]. On the contrary,

Eq. (12) introduces fluctuations in full phase space and let them develop spontaneously and continuously over time in a dynamical process.

In the Stochastic Mean Field (SMF) treatment [70] the fluctuations of the distribution function generated by the stochastic collision integral are projected on the coordinate space. Thus only local density fluctuations, which could be implemented as such in numerical calculations, are considered. The further assumption of local thermal equilibrium is made, with the possibility to derive analytical expressions for the density fluctuations. This implies that fluctuations can be implemented only when, after the first collision instants, the phase space occupancy is locally thermalized. In principle, thermal fluctuations could be introduced directly in the phase space, i.e. implementing $\sigma_f^2 = \bar{f}(1 - \bar{f})$ locally in the phase space. However, this is a difficult numerical task because of the high dimension of the phase space. In the standard application of the SMF method therefore one considers density fluctuations in a volume V :

$$\sigma_\rho^2(\mathbf{r}, t) = \frac{1}{V} \int \frac{d\mathbf{p}}{h^3/4} \sigma_f^2(\mathbf{r}, \mathbf{p}, t). \quad (15)$$

This variance could be directly calculated from the value of the average one-body distribution function provided by the BUU simulation, and fluctuations be introduced accordingly. However it is more practical to have explicit analytical expressions for the density fluctuations. Within the assumption of local thermal equilibrium, the mean distribution function can be parametrized by the expression $f(\mathbf{r}, \mathbf{p}, t) = 1/(1 + \exp(e - \mu(\mathbf{r}, t))/T(\mathbf{r}, t))$ with a local chemical potential and temperature $\mu(\mathbf{r}, t)$ and $T(\mathbf{r}, t)$, respectively, and with $e = p^2/2m$. Introducing the expression for the fluctuation variance into Eq.(15) one obtains, after some algebra:

$$\sigma_\rho^2 = \frac{1}{V} \frac{2\pi m \sqrt{(2m)} T}{h^3/4} \int \frac{1}{\sqrt{e}} \frac{1}{1 + \exp(e - \mu)/T} de \quad (16)$$

We note that Eq.(16) is consistent with the thermodynamical relation for the variance of the particle number in a given volume. To obtain a more explicit expression, and to eliminate the chemical potential we can use the Sommerfeld expansion, for the function f around $e = \mu$ for small T/ϵ_F ratio, being ϵ_F the Fermi energy at the considered density. We then obtain

$$\sigma_\rho^2 = \frac{16\pi m \sqrt{(2m)}}{h^3 V} \sqrt{\epsilon_F} T \left[1 - \frac{\pi^2}{12} \left(\frac{T}{\epsilon_F} \right)^2 + \dots \right]. \quad (17)$$

The procedure can be considered and implemented separately for neutrons and protons.

2.5 QMD models

Molecular dynamics (QMD) approaches are widely employed to describe the nuclear reaction dynamics (several examples can be found in Refs.[32, 37, 38]). Within such a family of models, the nuclear many-body state is written as a product of single particle states, usually represented by Gaussian wave packets. Two-body collisions between nucleon packets are treated stochastically, by choosing randomly the scattering angle associated with the n-n scattering process. Moreover, the localization of the wave packets induces some additional correlations also in the mean-field propagation. Then these approaches are very well suited to enable the formation of clusters and fragments.

In QMD, the one-body distribution function is obtained as a sum of Gaussian wave packets:

$$f_{QMD}(\mathbf{r}, \mathbf{p}, t) = \sum_{k=1}^A \left(\frac{2\nu}{\pi} \right)^{3/2} e^{-2\nu(\mathbf{r} - \mathbf{R}_k(t))^2} (2\pi\hbar)^3 \delta(\mathbf{p} - \mathbf{P}_k(t)), \quad (18)$$

where ν , or $\Delta x = (4\nu)^{-1/2}$, is a fixed parameter representing the width of the wave packet of each nucleon. The centroids of the wave packets (\mathbf{R}_k and \mathbf{P}_k) are propagated according to classical equations

of motion (Hamilton equations), with the Hamiltonian evaluated starting from the effective interaction considered and the nucleon distribution given by Eq.(18).

As far as the collision integral is concerned, similarly to the approach introduced before, the in-medium n-n cross sections $d\sigma/d\Omega$ is employed to evaluate the probability for a nucleon-nucleon collision to occur. More specifically, a pair of nucleons represented by $(\mathbf{R}_i, \mathbf{P}_i)$ and $(\mathbf{R}_j, \mathbf{P}_j)$ will collide when the radial distance among them becomes minimum during the considered time step interval Δt and this closest distance is less than $\sqrt{\sigma/\pi}$, in analogy with the geometrical prescription by Bertsch and Das Gupta [29]. This implies that nucleons collide at a given finite relative distance, whereas in the BUU equation, distribution functions are evaluated at the same point \mathbf{r} in configuration space, i.e. collisions are local in space.

The main general drawback of QMD approaches is that the one-body distribution f_{QMD} of Eq.(18) does not preserve the Pauli principle along the dynamical evolution, though it can be enforced in the initial conditions. As a consequence, the system can be pushed towards a classical type of behavior. Some methods have been proposed to cure this problem [37].

From the above discussion, we expect mean-field (BUU-like and stochastic) theories to better describe genuine mean-field effects, owing to the better mapping of the one-body distribution function in phase space. On the other hand, the effect of correlations is emphasized in QMD-like models, but the fermionic nature of the nuclear systems under study could be quickly lost along the dynamical evolution.

2.6 Antisymmetrized Molecular Dynamics

In the antisymmetrized molecular dynamics (AMD) approach, a system of A -nucleon is represented by a Slater determinant of Gaussian wave packets,

$$|\Phi_{AMD}(Z)\rangle = \hat{A} \prod_{K=1}^A \varphi_K \quad (19)$$

where \hat{A} is the full antisymmetrization operator. Each single-particle state φ_k is a product of a Gaussian function and a spin-isospin state

$$\langle \mathbf{r} | \varphi_k \rangle = \exp\left[-\nu\left(\mathbf{r} - \frac{\mathbf{Z}_k}{\sqrt{\nu}}\right)^2\right] \otimes \chi_{\alpha_k}. \quad (20)$$

The spin and isospin of each nucleon are kept fixed, $\alpha_k = p \uparrow, p \downarrow, n \uparrow$ or $n \downarrow$. The width parameter ν of the Gaussian function is chosen to be $\nu = 1/(2.5 \text{ fm})^2$ in almost all applications. It should be noticed that the single-particle states φ_k are not orthogonal to each other, however, as long as they are linearly independent, the Slater determinant (19) is a proper fermionic many-body state. The latter results parametrized in terms of the Gaussian centroids $Z = \{\mathbf{Z}_1, \mathbf{Z}_2, \dots, \mathbf{Z}_A\}$, which are complex vectors. The time-dependent variational principle allows to determine the following equations of motion:

$$\frac{d}{dt} \mathbf{Z}_k = \{\mathbf{Z}_k, \mathcal{H}\}_{PB}, \quad (21)$$

with the Poisson bracket (PB) suitably defined for the non-canonical variables Z [71, 72, 73]. The above equation accounts for the wave packet propagation in the mean field. The Hamiltonian \mathcal{H} is the expectation value of the Hamiltonian operator H and a suitable technique is adopted to subtract the spurious zero-point kinetic energies of fragment center-of-mass motions [35, 74]. Similarly to the transport approaches discussed above, an effective interaction is employed in AMD, such as the Gogny force or the Skyrme force.

A stochastic collision integral, describing hard two-body scattering between nucleon packets and preserving the antisymmetrization is explicitly included in the description.

As in QMD models, in AMD the width parameter ν is always kept fixed. On the other hand, in the fermionic molecular dynamics (FMD) model proposed by Feldmeier [33], the width parameters ν_k of the individual wave packets are treated as time-dependent. This generalization allows one to get the exact quantum-mechanical solution for free particle propagation and for the spreading of single-particle states. However, the fixed width choice looks more suitable to describe fragmentation events, thanks to the localization of the nucleon wave packet [34], as shown already by the very first applications of the AMD approach to the simulation of heavy ion collisions [35, 36]. However, further extensions of AMD also include the possibility to consider deformation of the wave packets, which actually can be represented as a superposition of many Gaussian wave functions, see Ref. [42] for a review.

A recent upgrade of the AMD model considers the possibility to include explicit light cluster production, as an extension of the nucleon correlations induced by the collision integral [75, 76]. The implementation of light clusters, up to mass $A=3$, was actually introduced first in the context of a BUU approach, leading to the pBUU model [77, 78].

2.7 Relativistic transport approaches

Within a fully relativistic picture, equilibrium and dynamical properties of nuclear systems at the hadronic level are well described by the the Quantum Hadro Dynamics (QHD) effective field model [79, 80, 44].

Such a framework provides consistent results for the nuclear structure of finite nuclei [81, 82, 45], for the NM Equation of State and liquid-gas phase transitions [83]. and for collective excitations [84, 85] and nuclear collision dynamics [86, 87].

2.7.1 QHD effective field theory

In QHD theory, the main dynamical degrees of freedom of the system are included by considering the nucleons coupled to the isoscalar scalar σ and vector ω mesons and to the isovector scalar δ and vector ρ mesons.

Hence the Lagrangian density for this approach, including non-linear isoscalar/scalar σ -terms [89], is given by:

$$\begin{aligned}
L = & \bar{\psi}[\gamma_\mu(i\partial^\mu - g_\omega V^\mu - g_\rho \mathbf{B}^\mu \cdot \vec{\tau}) - (M - g_\sigma\phi - g_\delta \vec{\tau} \cdot \vec{\delta})]\psi + \\
& \frac{1}{2}(\partial_\mu\phi\partial^\mu\phi - m_s^2\phi^2) - \frac{a}{3}\phi^3 - \frac{b}{4}\phi^4 - \frac{1}{4}W_{\mu\nu}W^{\mu\nu} + \frac{1}{2}m_\omega^2V_\nu V^\nu + \\
& \frac{1}{2}(\partial_\mu\vec{\delta} \cdot \partial^\mu\vec{\delta} - m_\delta^2\vec{\delta}^2) - \frac{1}{4}\mathbf{G}_{\mu\nu}\mathbf{G}^{\mu\nu} + \frac{1}{2}m_\rho^2\mathbf{B}_\nu\mathbf{B}^\nu
\end{aligned} \tag{22}$$

where $W^{\mu\nu}(x) = \partial^\mu V^\nu(x) - \partial^\nu V^\mu(x)$ and $\mathbf{G}^{\mu\nu}(x) = \partial^\mu \mathbf{B}^\nu(x) - \partial^\nu \mathbf{B}^\mu(x)$.

Here $\psi(x)$ is the nucleon fermionic field, $\phi(x)$ and $V^\nu(x)$ represent neutral scalar and vector boson fields, respectively, whereas $\vec{\delta}(x)$ and $\mathbf{B}^\nu(x)$ are the charged scalar and vector fields and $\vec{\tau}$ denotes the isospin matrices. The coefficients of the type m_i and g_i indicate masses and coupling constant of the different meson channels and M denotes the nucleon mass.

From the Lagrangian, Eq.(22), a set of coupled equations of motion for the meson and nucleon fields can be derived. The basic approximation in nuclear matter applications consists in neglecting all the terms containing derivatives of the meson fields with respect to the their mass contributions. Then the meson fields are simply connected to the operators of the nucleon scalar and current densities by the

following equations:

$$\widehat{\Phi}/f_\sigma + A\widehat{\Phi}^2 + B\widehat{\Phi}^3 = \bar{\psi}(x)\psi(x) \equiv \widehat{\rho}_S \quad (23)$$

$$\begin{aligned} \widehat{V}^\mu(x) &\equiv g_\omega V^\mu = f_\omega \bar{\psi}(x)\gamma^\mu\psi(x) \equiv f_\omega \widehat{j}_\mu, \\ \widehat{\mathbf{B}}^\mu(x) &\equiv g_\rho \mathbf{B}^\mu = f_\rho \bar{\psi}(x)\gamma^\mu \vec{\tau}\psi(x), \\ \widehat{\vec{\delta}}(x) &\equiv g_\delta \vec{\delta} = f_\delta \bar{\psi}(x)\vec{\tau}\psi(x) \end{aligned} \quad (24)$$

where $\widehat{\Phi} = g_\sigma \phi$, $f_\sigma = (g_\sigma/m_\sigma)^2$, $A = a/g_\sigma^3$, $B = b/g_\sigma^4$, $f_\omega = (g_\omega/m_\omega)^2$, $f_\rho = (g_\rho/m_\rho)^2$, $f_\delta = (g_\delta/m_\delta)^2$.

Exploiting Eqs.(23,24) for the meson field operators, it is possible to derive a Dirac-like equation for the nucleon fields which contains only nucleon field operators. This equation can be consistently solved within a Mean Field Approximation (Relativistic Mean Field, RMF), i.e. in a self-consistent Hartree scheme [80, 44].

Some attempts were performed to go beyond this scheme. In particular, it is interesting to notice that the inclusion of Fock terms automatically leads to contributions to the various meson exchange channels, also in absence of explicit direct coupling terms. A thorough study of these effects was performed in [88], for asymmetric nuclear matter.

2.7.2 Relativistic semi-classical transport equations

Within the previous assumptions, we move to discuss a kinetic approach which adopts the semi-classical approximation. This allows one to establish a formal connection to the transport models described above.

In the RMF model, the nuclear system is essentially described at the one-body level, with some correlation effects included, in an effective manner, through (density dependent) coupling constants. To derive the kinetic equations for the one-body nucleon density matrix, it is useful to introduce, in quantum phase-space, the Wigner function for the fermion field [90, 91]. The latter is defined as:

$$[\widehat{F}(x, p)]_{\alpha\beta} = \frac{1}{(2\pi)^4} \int d^4R e^{-ip \cdot R} \langle : \bar{\psi}_\beta(x + \frac{R}{2}) \psi_\alpha(x - \frac{R}{2}) : \rangle,$$

where α and β are double indices for spin and isospin. The brackets denote statistical averaging and the colons indicate normal ordering. The equation of motion can be derived from the Dirac field equation by using standard procedures (see e.g.[90, 91]).

Within the Hartree-Fock scheme and in the semi-classical approximation, one obtains the following kinetic equations [92, 88]:

$$\begin{aligned} \frac{i}{2} \partial_\mu \gamma^\mu \widehat{F}^{(i)}(x, p) + \gamma^\mu p_{\mu i}^* \widehat{F}^{(i)}(x, p) - M_i^* \widehat{F}^{(i)}(x, p) + \\ \frac{i}{2} \Delta \left[\tilde{f}_\omega j_\mu(x) \gamma^\mu \pm \tilde{f}_\rho j_{3\mu}(x) \gamma^\mu - \tilde{f}_\sigma \rho_S(x) \mp \tilde{f}_\delta \rho_{S3}(x) \right] \widehat{F}^{(i)}(x, p) = 0, \end{aligned} \quad (25)$$

where the Wigner function has been decomposed into neutron and proton components ($i = n, p$) and the upper (lower) sign corresponds to protons (neutrons). In the above equation $\Delta = \partial_x \cdot \partial_p$, with ∂_x acting only on the first term of the products, and $\rho_{S3} = \rho_{Sp} - \rho_{Sn}$ and $j_{3\mu}(x) = j_\mu^p(x) - j_\mu^n(x)$ are the isovector scalar density and baryon current, respectively. The kinetic momenta and effective masses are defined as:

$$\begin{aligned} p_{\mu i}^* &= p_\mu - \tilde{f}_\omega j_\mu(x) \pm \tilde{f}_\rho j_{3\mu}(x), \\ M_i^* &= M - \tilde{f}_\sigma \rho_S(x) \pm \tilde{f}_\delta \rho_{S3}(x), \end{aligned} \quad (26)$$

where the effective coupling functions $\tilde{f}_i (i = \sigma, \omega, \rho, \delta)$ have been introduced. The latter are generally space, i.e. density, dependent. Within the Hartree-Fock approximation, the effective coupling constants incorporate the Fock term contributions, and get finite values in all channels, even in absence of direct contributions. It is easy to realize that the common RMF approximation (Hartree level) is recovered from the Hartree-Fock results by changing the effective coupling functions \tilde{f}_i to the explicit coupling constants f_i .

The explicit effect of two-body correlations can be included also within the relativistic covariant framework. Eq.(25) can be complemented by a two-body collision integral, to explicitly take into account effects beyond the mean-field picture (RBUU models) [59].

3 Effective interactions and symmetry energy

In the following we will review results obtained with both classes of models discussed in Section 2. A common ingredient is certainly the nuclear effective interaction, from which the nuclear EOS can be derived in the equilibrium limit. The comparison of suitable reaction observables, evaluated in simulated transport model events, to experimental data would allow one to extract information on relevant nuclear matter features.

For illustrative purposes, let us consider, as a standard effective interaction, a Skyrme interaction, with the energy density \mathcal{E} expressed in terms of the isoscalar, $\rho = \rho_n + \rho_p$, and isovector, $\rho_3 = \rho_n - \rho_p$, densities and kinetic energy densities ($\tau = \tau_n + \tau_p, \tau_3 = \tau_n - \tau_p$) as [93]:

$$\begin{aligned} \mathcal{E} = & \frac{\hbar^2}{2m} \tau + C_0 \rho^2 + D_0 \rho_3^2 + C_3 \rho^{\alpha+2} + D_3 \rho^\alpha \rho_3^2 + C_{eff} \rho \tau \\ & + D_{eff} \rho_3 \tau_3 + C_{surf} (\nabla \rho)^2 + D_{surf} (\nabla \rho_3)^2. \end{aligned} \quad (27)$$

The coefficients $C_{..}, D_{..}$ are combinations of the traditional Skyrme parameters [94]. The nuclear mean-field potential U_q ($q = n, p$), which enters the transport equations, is consistently derived from the energy functional \mathcal{E} .

The isoscalar section of the energy functional is usually fixed requiring that the saturation properties of symmetric nuclear matter, with a compressibility modulus around $K \approx 200 - 250 MeV$, are reproduced.

Many discussions will concentrate on the nuclear symmetry energy E_{sym} , that we define starting from the expression of the energy per nucleon: $E(\rho, \rho_3)/A \equiv E(\rho)/A + \frac{E_{sym}(\rho)}{A} (\rho_3/\rho)^2 + O(\rho_3/\rho)^4 + \dots$

E_{sym}/A gets a kinetic contribution directly from basic Pauli correlations and a potential part, $C_{pot}(\rho)$, from the highly controversial isospin dependence of the effective interactions. At zero temperature:

$$\frac{E_{sym}}{A} = \frac{E_{sym}}{A} (kin) + \frac{E_{sym}}{A} (pot) \equiv C_{sym}(\rho) = \frac{\epsilon_F}{3} + C_{pot}(\rho) \quad (28)$$

The coefficient $C_{sym}(\rho)$ can be written as a function of the Skyrme coefficients:

$$C_{sym}(\rho) = \frac{\epsilon_F}{3} + D_0 \rho + D_3 \rho^{\alpha+1} + \frac{2m}{\hbar^2} \left(\frac{C_{eff}}{3} + D_{eff} \right) \epsilon_F \rho, \quad (29)$$

with ϵ_F denoting the Fermi energy at density ρ and m the nucleon mass. It is often convenient to expand the symmetry energy $C_{sym}(\rho)$ around its value at the saturation density ρ_0 :

$$C_{sym}(\rho) = S_0 + \frac{L}{3} \left(\frac{\rho - \rho_0}{\rho_0} \right) + \frac{K_{sym}}{18} \left(\frac{\rho - \rho_0}{\rho_0} \right)^2, \quad (30)$$

where S_0 (ofted denoted also as J) indicates the symmetry energy value at normal density, whereas L and k_{sym} are related to first and second derivative, respectively.

As an example, we illustrate here some results associated with the recently introduced SAMi-J Skyrme effective interactions [96], which provide a variety of trends for the nuclear symmetry energy. The corresponding parameters are determined from a fitting protocol which accounts for the following properties: binding energies and charge radii of some doubly magic nuclei - which allow the SAMi-J family to predict a reasonable saturation density ($\rho_0 = 0.159 \text{ fm}^{-3}$), energy per nucleon $E/A(\rho_0) = -15.9 \text{ MeV}$ and incompressibility modulus ($K = 245 \text{ MeV}$) of symmetric nuclear matter -; some selected spin-isospin sensitive Landau-Migdal parameters [97]; the neutron matter EOS of Ref.[98].

Let us consider three SAMi-J parametrizations: SAMi-J27, SAMi-J31 and SAMi-J35 [96]. Since, as mentioned above, Skyrme interactions are usually fitted in order to reproduce the main features of selected nuclei, the symmetry energy coefficient takes, for the three parametrizations, the same value, $C_{sym}(\rho_c) \approx 22 \text{ MeV}$, at the density $\rho_c \approx 0.6\rho_0$, which can be considered as the average density of medium-size nuclei. Then the value, J , of the symmetry energy at saturation density is different in the three cases, being equal to 27 MeV (SAMi-J27), 31 MeV (SAMi-J31) and 35 MeV (SAMi-J35), respectively. The values of the slope parameter $L = 3\rho_0 \left. \frac{dC_{sym}(\rho)}{d\rho} \right|_{\rho=\rho_0}$ are equal to $L = 29.9 \text{ MeV}$ (SAMi-J27), $L = 74.5 \text{ MeV}$ (SAMi-J31) and $L = 115.2 \text{ MeV}$ (SAMi-J35). The corresponding density dependence of $C_{sym}(\rho)$ is shown in Fig.3(a). It would be interesting to explore the effects of these interactions, which provide a nice reproduction of nuclear ground state and structure properties, also in transport simulations [99, 100, 101].

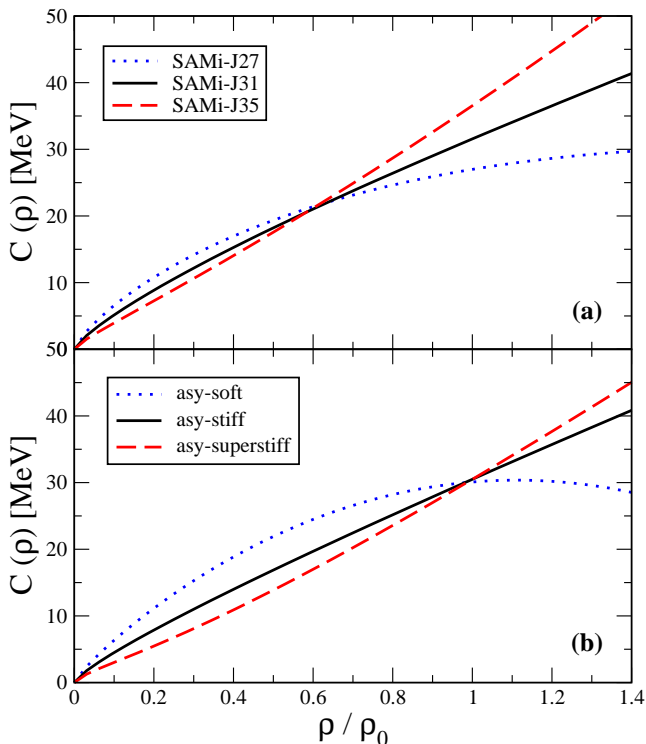


Figure 3: (Color online) (a) Three effective parameterizations of the symmetry energy, as given by the Skyrme SAMi-J family [96]. (b) Parametrizations corresponding to momentum independent interactions: asystiff (dotted line), asysoft (full line) and asysuperstiff (dashed line) [46].

For a comparison, Fig.3(b) illustrates three different parameterizations of $C_{sym}(\rho)$ corresponding to momentum independent Skyrme interactions widely employed in the literature: the asysoft, the asystiff and asysuperstiff respectively, see [46] for a detailed description. The latter interactions are mainly fitted on nuclear matter properties, thus the symmetry energy curves crosses at normal density ($\rho = \rho_0$). The sensitivity of the simulation results can be tested against these different choices. We also mention that some transport models employ the following parametrization for the potential part of the symmetry energy: $C_{pot}(\rho) \approx 17.5(\rho/\rho_0)^{\gamma_i}$. In this case, the stiffness of the symmetry energy is obviously determined by the exponent γ_i .

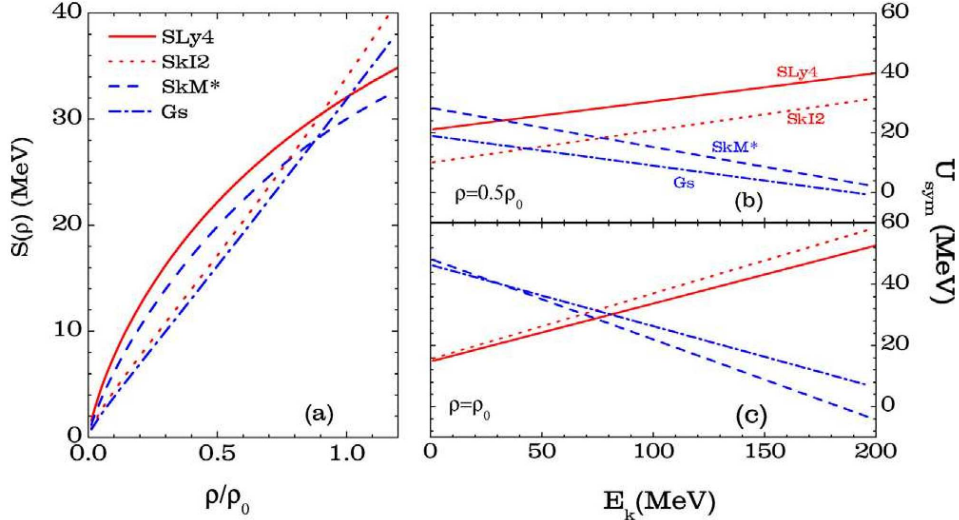


Figure 4: (Color online) (a) Density dependence of symmetry energy, (b) energy dependence of the Lane potential at $\rho = 0.5\rho_0$ and (c) $\rho = \rho_0$, for the Skyrme parametrizations SLy4 (solid line), SkI2 (dot line), SkM* (dash line) and Gs (dot dash line). Taken from [102].

It should be noted that the Skyrme mean-field potential exhibits a quadratic momentum dependence, which can be considered as a good approximation in low momentum regions [95]. In asymmetric NM, the momentum dependence of the neutron/proton mean-field potentials leads to the splitting of neutron and proton effective masses.

According to the strength of the momentum dependent terms, the SAMi-J interactions lead to an effective isoscalar nucleon mass $m^*(I = \rho_3/\rho = 0) = 0.67 m$ and a neutron-proton effective mass splitting $m_n^* - m_p^* = 0.023 mI$ MeV at saturation density. This small splitting effect is associated with a quite flat momentum dependence of the symmetry potential. We note that a steeper decrease at high momenta is suggested from the optical model analysis of nucleon-nucleus scattering data performed in [95]. This feature should not impact nuclear structure properties and low energy reactions, where one mainly explores the low-momentum region of the symmetry potential (i.e., the region below and around the Fermi momentum).

A recent illustration of several possible combinations of symmetry energy and effective mass splitting trends is found in Ref.[102], still in the context of Skyrme interactions. Fig.4 represents four Skyrme parametrizations which lead to a soft or a stiff behavior of the symmetry energy. The right panel of the figure shows the energy dependence of the Lane potential U_{sym} , which is related to the difference between neutron and proton mean-field potentials, at two fixed density values. One can see that the parameters of the Skyrme interactions can be tuned in such a way that, for a given symmetry energy trend, one can obtain a decreasing (increasing) trend, with the energy, of the Lane potential, corresponding to proton effective mass smaller (greater) than neutron effective mass.

New perspectives towards a more general formulation of the density and isospin dependence of the nuclear EOS are provided by metamodeling [103]. This is a flexible approach that can interpolate continuously between existing EOS and allow a more global analysis of the relation between experimental constraints and EOS features. It would be interesting to follow the same philosophy for the effective interactions employed in transport models.

The discussion about symmetry energy and effective masses is quite relevant also within a relativistic framework. Effective interactions which are commonly employed in the relativistic frame are the so-

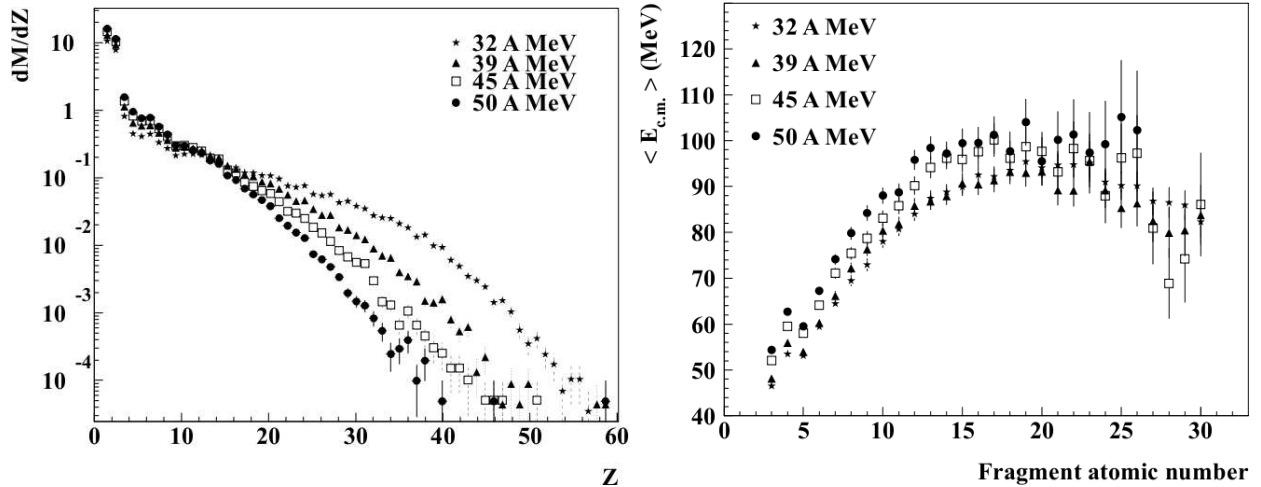


Figure 5: Left panel: Charge distributions of fragments produced in central collisions of Xe + Sn at four incident energies: 32, 39, 45, and 50 A MeV. Right panel: Average center of mass kinetic energy of the fragments produced in the same reactions, as a function of their atomic number. The statistical error bars are shown. Adapted from [12], with kind permission of the APS.

called $NL\rho$ (where the isovector-scalar δ coupling is set to zero) and $NL\rho\delta$ interactions, see Ref.[46] for more details. Actually one observes that the two effective couplings, vector and scalar, in the isovector channel influence in a different way the static (symmetry energy) and dynamic (collective response, reaction observables) properties of asymmetric nuclear matter. Hence reaction dynamics studies can be useful also to solve the open problem of the determination of the (scalar- and vector-) isovector coupling, in connection to symmetry energy and effective mass splitting. In particular, the contributions to the scalar-isovector channel are mainly coming from correlation effects [88], thus it would be desirable to employ, within the QHD-RMF framework, effective coupling constants derived from microscopic Dirac-Brueckner-Hartree-Fock (DBHF) calculations. Several attempts have been performed, see [104, 105] for instance, but the results still exhibit some degree of model dependence.

4 Reaction dynamics at medium energy: central collisions

In the Fermi energy regime (30-60 A MeV), different reaction mechanisms are explored, according to the reaction centrality, in heavy ion collisions, ranging from (incomplete) fusion and deep-inelastic binary processes, up to fragmentation of the projectile-target overlap region (the neck region) and multifragment production. In very central collisions, the degree of stopping is such as to lead to the formation of a unique composite source [106, 107, 108, 73] with a temperature in the range of $T \approx 3$ -5 MeV, which eventually breaks up into many pieces, as a result of thermal effects and of the compression-expansion dynamics. Indeed, as a quite interesting feature, this process is also accompanied by the development of a radial flow, which characterizes the kinematical properties of the reaction products [12, 109]. These features are summarized in Fig.5, which represents the evolution of fragment charge distribution and kinetic energies, as measured for the system $^{129}\text{Xe} + ^{\text{nat}}\text{Sn}$ at different beam energies. From the left panel one can appreciate how the fragmentation process evolves with the energy transferred to the system, with smallest fragments produced at the highest beam energy. The right panel of the figure shows clearly that, excluding from the analysis the heaviest fragments, the mean kinetic energy per nucleon exhibits an almost linear increase with the fragment charge. This trend can be interpreted as an evidence of the presence of a radial collective flow, leading to similar radial velocities for all fragments (and thus to a kinetic energy scaling with the fragment mass).

From the experimental observations outlined above, one can already figure out that the occurrence of surface and/or volume instabilities may play a central role in the description of the reaction path. Simulations of the multifragmentation dynamics based on transport models have allowed, through the comparison with experimental data, to shed light on the compression-expansion dynamics, yielding independent information on the nuclear matter compressibility [110]. We illustrate here a selection of simulation results related to central collisions at Fermi energies. Emphasis will be put on the features of the fragmentation process, in connection to the treatment employed to describe the many-body dynamics, and on aspects related to isospin transport and isotopic features of the reaction products.

4.1 Pre-equilibrium nucleon and cluster emission

During the first stage of the reaction, hard two-body scattering plays an essential role and pre-equilibrium emission is observed, i.e. nucleons and light particles are promptly emitted from the system. One may expect that two- and higher order correlations play an important role in determining mass, isotopic properties and kinematical features of the particles emitted. Moreover, it is easy to realize that this stage influences significantly also the following evolution of the collision. Indeed, the amount of particles and energy removed from the system affects the properties of the composite source that eventually breaks up into pieces. Hence, when discussing multifragmentation mechanisms, a detailed analysis of this early emission is in order. Moreover, pre-equilibrium emission, involving energetic particles, is particularly sensitive also to the momentum dependence of the nuclear effective interaction.

To get an insight into the theoretical description of the reaction dynamics, it is quite instructive to compare the results obtained, for selected collisions at Fermi energy, within the scheme of the AMD and SMF models (employing similar momentum dependent interactions and n-n cross section parametrizations in the two cases). This analysis was performed in Ref.[43], for the neutron-poor $^{112}\text{Sn}+^{112}\text{Sn}$ and neutron-rich $^{124}\text{Sn}+^{124}\text{Sn}$ reactions, at 50 MeV/nucleon. As far as the early emission of nucleons and light clusters is concerned, one observes that these particles (with mass number $A \leq 4$) leave the system mostly in the time interval between ≈ 70 -120 fm/c (see also Fig.9). A striking difference between the two models concerns the amount of these emitted particles, that is larger in the SMF case, though the average kinetic energy of this emission is similar in the two models (being 20.72 MeV/nucleon in SMF and 21.95 MeV/nucleon in AMD) [43]. Moreover, mainly unbound nucleons are emitted in the SMF case. However, it should be noticed that, in AMD, also light fragments, with mass number $5 \leq A \leq 15$, leave the system during the early stage of the reaction, on equal footing as light particles. This is not observed in SMF. Thus, as a matter of fact, the total amount of mass which escapes from the system is close in the two models. As a consequence, we also expect a similar global amount of mass going into the production of intermediate mass fragments (IMF), with mass number $A > 15$, as it will be discussed in the following.

As argued in Ref.[43], the difference observed between the two models for single nucleon and light particle emission can be ascribed to the fact that clustering effects and many-body correlations are more efficient in AMD, due to the nucleon localization, reducing the amount of mass that goes into very light reaction products. Some effects may also be connected to a different compression-expansion dynamics in the two models, as we will discuss below. Clustering effects are under intense investigation nowadays, in a variety of contexts, including astrophysical environments [7], and it deserves much attention to get new insights from multifragmentation events [73, 76, 61, 111].

4.1.1 Isospin effects

A lot of interest in the last years has been directed also to the isotopic composition of the pre-equilibrium emission. This appears as a rather interesting feature, which is expected to be particularly sensitive to the isovector channel of the effective interaction and, namely, to the symmetry energy. Because

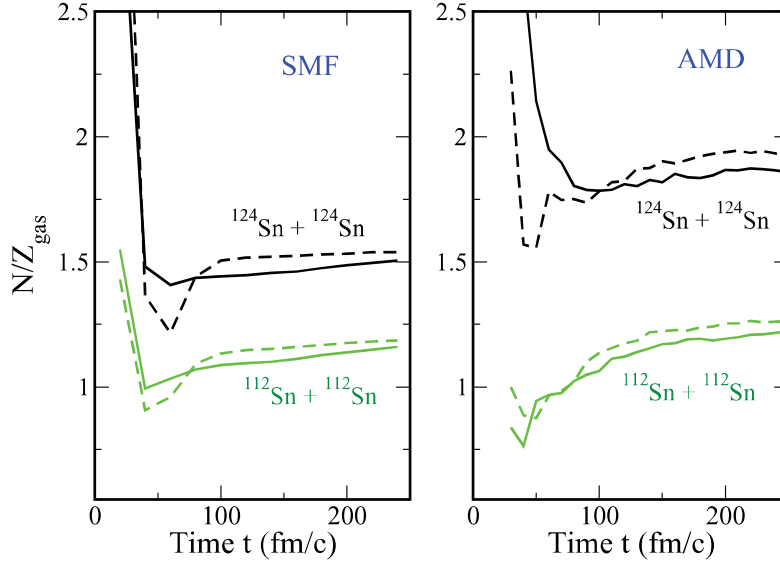


Figure 6: (Color online) Time evolution of the N/Z content of the pre-equilibrium emission, as obtained in SMF (left panel) and AMD (right panel) models, for the $^{112}\text{Sn} + ^{112}\text{Sn}$ and $^{124}\text{Sn} + ^{124}\text{Sn}$ reactions. Solid lines, asy stiff interaction; dashed lines, asy soft. Taken from [43].

the symmetry energy is density dependent, this kind of observables are also rather useful to track the reaction dynamics itself. Moreover, also isotopic features are expected to be sensitive, generally speaking, to correlations and clustering effects. The comparison between AMD and SMF results, for $^{124}\text{Sn} + ^{124}\text{Sn}$ and $^{112}\text{Sn} + ^{112}\text{Sn}$ reactions at 50 MeV/A is shown in Fig.6, when employing a soft or a stiff symmetry energy parametrization. One can observe that the more abundant pre-equilibrium emission obtained in SMF is associated with a lower N/Z value, with respect to the AMD results, especially for the neutron-rich system. Both effects could be connected to the more pronounced clustering effects in AMD and/or the different density conditions explored along the reaction path. Indeed, if cluster production is favored, protons are more likely bound in it.

Some general considerations emerge from the results displayed in the figure: when comparing the two reactions, it is seen that neutron (proton) emission is more abundant in the neutron-rich (poor) systems, as expected. Moreover, the figure also shows that a larger (smaller) number of neutrons (protons) is emitted in the asy soft case, as compared to the asy stiff case. This is consistent with the larger repulsion of the symmetry potential for the soft parametrization below normal density. Hence this result confirms that pre-equilibrium particles leave the system from regions that are at sub-normal density, where the symmetry energy is higher in the soft case (see Fig. 3). In spite of these common features, one can easily notice that the quantitative differences between the AMD and SMF result obtained for a given parametrization are larger than the differences given by the two parametrizations. This observation highlights the important impact of the description of the many-body dynamics, namely the interplay between mean-field and correlation effects, even on isospin observables. A correct description of clustering effects looks crucial in order to extract reliable information on the low-density symmetry energy behavior from pre-equilibrium observables.

An insight into effects related to the momentum dependence of the nuclear interaction is got by looking at the N/Z ratio versus the kinetic energy of the pre-equilibrium emitted particles. As an illustrative example, we show here the results discussed in Ref.[102], obtained with the ImQMD model, see Fig.7. The figure displays the ratio of the yields of neutrons and protons, for the same reactions considered above (at 50 MeV/nucleon), as a function of the kinetic energy. Four Skyrme effective interactions are employed, corresponding to different symmetry energy parametrization (stiff or soft) and different splitting of the proton/neutron effective masses (see also Fig.4). One observes that,

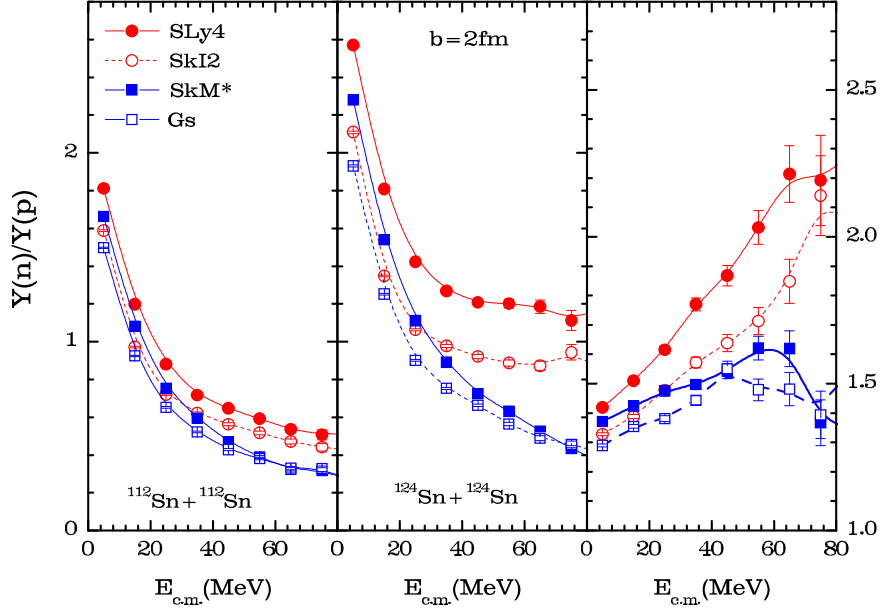


Figure 7: (Color online) Left panel: Neutron-proton ratio $Y(n)/Y(p)$ as a function of the kinetic energy for $^{112}\text{Sn} + ^{112}\text{Sn}$ at $b=2$ fm with angular cuts $70^\circ < \theta_{c.m.} < 110^\circ$; Middle panel: the same quantity, for $^{124}\text{Sn} + ^{124}\text{Sn}$. Right panel: Double ratios, $DR(n/p)$, as a function of kinetic energy. The results shown on the figure are for SLy4 (solid circles), SkI2 (open circles), SkM* (solid squares) and Gs (open squares). Taken from [102].

whereas the N/Z ratio of the particles emitted at low kinetic energies is governed by the low-density symmetry energy behavior (being larger in the soft case), the trend at large kinetic energy reflects the effective mass splitting sign. Higher N/Z values (see especially the case of the $^{124}\text{Sn} + ^{124}\text{Sn}$ system, middle panel) are associated with parametrizations having $m_n^* < m_p^*$. Indeed the latter case corresponds to a more repulsive symmetry potential for neutrons. This effect is particularly evident on the right panel, which represents the double ratio $DR(n/p)$, i.e. the ratio between the N/Z content of the pre-equilibrium emission obtained in the two systems considered (the neutron-rich $^{124}\text{Sn} + ^{124}\text{Sn}$ and the neutron poor $^{112}\text{Sn} + ^{112}\text{Sn}$). There have been recent attempts to compare predictions related to pre-equilibrium observables to experimental data, aiming at extracting information on symmetry energy and effective mass splitting sign at once. We report here, as an example, the results of Ref.[112], where simulations are still performed with the ImQMD model, employing the “soft” parametrizations of Fig.4. The double ratio $DR(n/p)$, evaluated for the same systems considered above at two beam energies, 50 and 120 MeV/nucleon, is represented in Fig.8. The comparison to the corresponding experimental data seems to favour the $m_n^* < m_p^*$ scenario. As already discussed above, in this case an increasing trend of the double n/p ratio with the kinetic energy is expected (see Fig.7).

4.2 Multifragment emission

As a result of the initial compression/expansion dynamics and/or thermal effects, the composite sources formed in central heavy ion collisions may reach low density values, attaining the co-existence zone of the nuclear matter phase diagram. A qualitative illustration of the corresponding reaction path is given in Fig.9 for the system $^{112}\text{Sn} + ^{112}\text{Sn}$ at 50 MeV/nucleon.

In this situation, as a possible scenario (see the recent review, Ref.[108]), the system undergoes a spontaneous phase separation, breaking up into several fragments, as a consequence of the occurrence of mean-field spinodal instabilities [113, 23]. This scenario is supported by simulations performed with stochastic mean-field models [114].

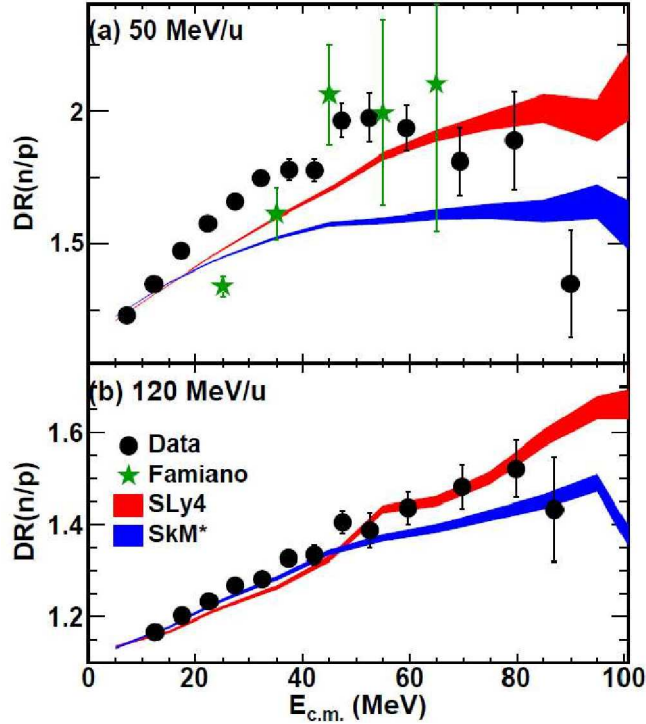


Figure 8: (Color online) Neutron to proton double ratio, for Sn + Sn collisions at beam energies $E_{beam}/A=50$ MeV (a) and 120 MeV (b). Experimental data are confronted with ImQMD transport calculations employing two different Skyrme interactions. Reprinted from [112], with kind permission of the APS.

It should be noticed, however, that in the initial high density phase nucleon correlations are expected to be rather large, owing to the huge amount of two-body nucleon-nucleon collisions. Hence some memory of these high density correlations could be kept along the fragmentation process, even assuming that clusters emerge essentially from the occurrence of mean-field instabilities. In any case, fluctuations of the one-body density induced by two-body scattering provide, at least, the initial seeds for the nucleon assembly into clusters. As already discussed in the case of pre-equilibrium observables, an insight into the interplay between mean-field and correlation effects can be got comparing the results of extended BUU-like models, including fluctuations, and molecular dynamics models. In the following we come back to the comparison performed between AMD and SMF calculations in Ref.[43], briefly discussing the main results. As already pointed out in subsection 4.1, in the AMD approach clustering effects appear

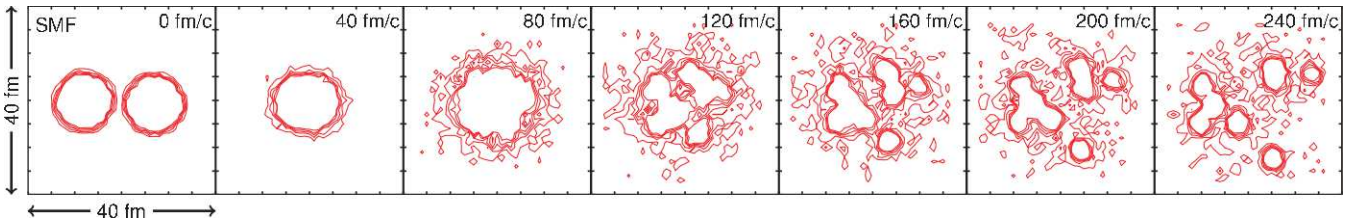


Figure 9: Contour plots of the density projected on the reaction plane, calculated with the SMF model, for the central reaction $^{112}\text{Sn} + ^{112}\text{Sn}$ at 50 MeV/nucleon, at several times (fm/c). The lines are drawn at projected densities beginning at 0.07 fm^2 and increasing by 0.1 fm^2 . The size of each box is 40 fm. Taken from [43].

to be more relevant, reducing the amount of free nucleons emitted, compared to SMF, in favor of a richer production of primary light IMFs. However, it is quite interesting to notice that the yield of sizeable

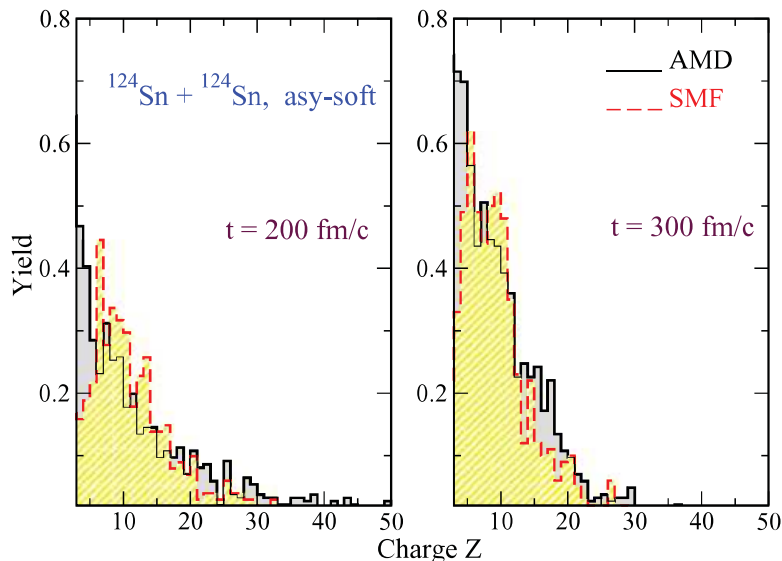


Figure 10: (Color online) Charge distribution as obtained in AMD (solid histogram) and in SMF (dashed histogram), for the reaction $^{124}\text{Sn} + ^{124}\text{Sn}$ at the time instant $t=200$ fm/c (left) and $t=300$ fm/c (right). Taken from [43].

primary IMFs ($Z > 6$) is rather close in the two models, likely keeping the fingerprints of low-density mean-field dynamics. This is shown in Fig.10, which compares the charge distributions obtained for the reaction $^{124}\text{Sn} + ^{124}\text{Sn}$ at 50 MeV/A. Looking more in detail, in SMF fragments with charge around $Z = 10$ are slightly more abundant, while in AMD the tail at larger Z (around 20) is more pronounced. The shape of the SMF charge distribution is closer to the expectations of spinodal decomposition [23]. However, it should be noticed that these differences are likely smoothed by secondary decay effects. In fact, both models are able to fit experimental IMF charge distributions reasonably well [71, 114]. A good reproduction of experimental data is provided also by QMD calculations, see Ref.[115]. A more refined analysis, based on event-by-event fragment correlations would be needed to disentangle among possible different fragmentation scenarios [107].

Major differences among models are connected to fragment kinematical properties: for instance, in SMF fragment kinetic energies are smaller, compared to AMD, by about 20%. These observations corroborate the scenario of a faster fragmentation process in AMD, while in SMF the system spends a longer time as a nearly homogeneous source at low density, thus quenching radial flow effects before fragment formation sets in [109, 114]. This delay in the fragmentation process, probably associated with the approximate treatment of fluctuations in SMF, could be overcome in upgraded stochastic mean-field models, introduced more recently [64, 66]. We review here some results obtained with the BLOB model.

The latter was conceived with the purpose of including fluctuations in full phase space, thus improving the treatment of fluctuations and correlations, but preserving, at the same time, mean-field features such as the proper description of spinodal instabilities at low density [116]. The improvement introduced by the BLOB approach is primarily providing a correct sampling of the fluctuation amplitude in full phase space, yielding a faster fragmentation dynamics and also a consistent description of the threshold toward multifragmentation. Fig. 11 shows results of simulations performed for the system $^{136}\text{Xe} + ^{124}\text{Sn}$, at several incident energies, analysed for central impact parameters at the time $t = 300$ fm/c. It is observed that fragmentation events start competing with the predominant low-energy fusion mechanism already at around 20 MeV/nucleon of beam energy. The multiplicity of the primary IMF with $Z > 4$, evaluated at 300 fm/c (full blue line), tends to grow with the beam energy, however a maximum at around 45 MeV/nucleon is observed when considering cold fragments, i.e. after the secondary de-excitation stage has been taken into account. (The cooling of the hot system is undertaken

by the use of the decay model Simon [117].) On the other hand, calculations performed with SMF, also shown on the figure, tend to overestimate the energy threshold toward multifragmentation.

In the figure, two experimental points from INDRA [118, 119] indicate the IMF multiplicity extracted from the analysis of central compact sources; they can be compared to the calculated cold distribution and indicate that the BLOB simulation, performed employing a soft EOS (with compressibility $K = 200$ MeV), is quantitatively consistent. The faster BLOB dynamics also leads to a better description of fragment kinetic energies, as recently pointed out in Ref.[121] in the case of fragmentation events emerging from mass-asymmetric reactions at Fermi energies, of recent experimental interest.

New improvements have been reported also in the case of the latest version of the AMD model, which includes a refined treatment of light cluster dynamics [75, 76]. Fig.12 reports a comparison of the calculated charge distribution, for central collisions (with impact parameter $0 < b < 2$ fm), with the INDRA data, for the system $^{129}\text{Xe} + ^{nat}\text{Sn}$ at 32 (right panel) and 50 (left panel) MeV/nucleon. It is interesting to see that the inclusion of cluster correlations leads to a quite good reproduction of the whole charge distribution spectrum, including protons and very light clusters [76].

4.2.1 Isotopic features

It is quite well established that, in neutron-rich systems, the fragment formation mechanism also keeps the fingerprints of the isovector channel of the nuclear effective interaction, in connection to the symmetry energy term of the EOS [47, 48]. Indeed one observes that the clusters (liquid drops) which

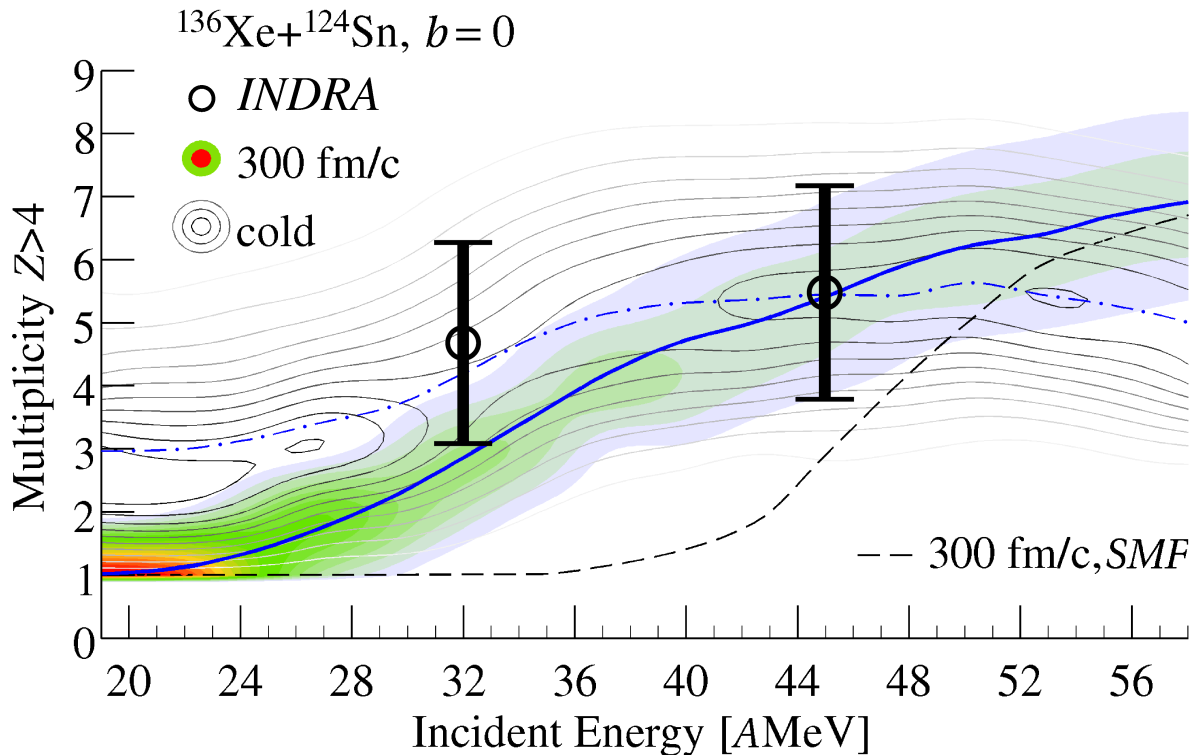


Figure 11: (Color online) BLOB simulation: evolution of IMF ($Z > 4$) multiplicity, as a function of incident energy for the system $^{136}\text{Xe} + ^{124}\text{Sn}$ and a selection of central collisions at 300fm/c (colour shades) and for the cold system (grey contours). Corresponding mean values are indicated for the BLOB simulation (full blue line for primary fragments and dot-dashed line for final fragments) and for a SMF calculation (black dashed line, primary fragments). Corresponding experimental data from Indra experiments [118, 119] are added for comparison, with average (symbols) and variance (bars) of the multiplicity distributions. Taken from [120].

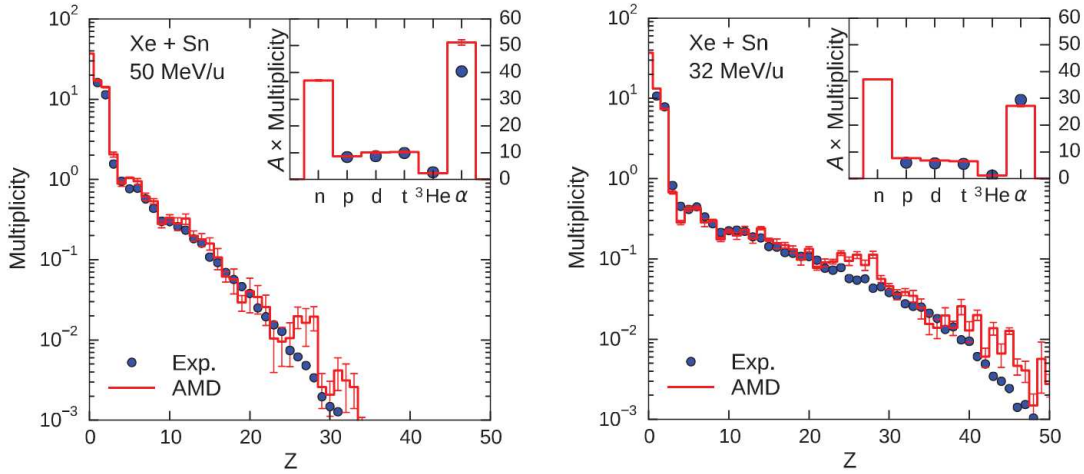


Figure 12: (Color online) Fragment charge distribution in central Xe+Sn collisions at the incident energies of 50 (left) and 35 (right) MeV/nucleon, calculated by AMD with cluster correlations. The inset shows the multiplicities of light particles multiplied by the mass number. The INDRA experimental data are taken from ref.[12]. Taken from [76].

emerge from the low-density nuclear matter have a lower N/Z ratio, with respect to the surrounding nucleons and light particles. This effect, the so-called isospin distillation (or fractionation), is connected to the density derivative of the symmetry energy and leads to the minimisation of the system potential energy [122, 123, 46]. Fluctuations act on both isoscalar and isovector degrees of freedom. On top of the average isospin distillation mechanism, isovector fluctuations generate the isotopic distribution of the fragments observed. Combining the two features, namely the average fragment N/Z and the corresponding variance, it should be possible to grasp the behavior of the low-density symmetry energy, see the analysis in Ref.[125]. This has been done also resorting to the so-called isoscaling analysis [122, 124]. As an illustrative example, Fig.13 shows the action of the isovector terms on the system $^{136}\text{Xe}+^{124}\text{Sn}$ (at 32 MeV/A), looking at fragment isotopic features. Results obtained with BLOB, employing an asystiff EOS, are displayed [116].

To explore the behavior of the system as a function of the local density, ripples of the mean-field potential, which can be considered as pre-fragments, are identified at several time instants along the dynamical evolution of the nuclear reaction. Then isospin effects are investigated as a function of the average local density and for different ripple sizes. Different sets of potential-concavity sizes are indicated by extracting a corresponding mass A' . As one can see from the bottom panel of the figure, from an initial situation where the system is close to saturation density and the average isospin is determined by the mixing of target and projectile nuclei, densities drop to smaller values and the isospin distribution extends over a large range. In particular, the smaller is the local density, the larger is the neutron content measured in corresponding sites, as neutrons favour the most volatile phase.

The top panel of the figure shows the isotopic distribution obtained, at two different times, for fragments in two different mass ranges A' . Considering that, at the instants considered, thermal equilibrium is attained, the distribution of the difference $\delta = (N' - Z')$ with respect to its average is expected to behave as: $P(\delta) \approx \exp[-(\delta^2/A')C_{sym}(\rho_{well})/T]$, thus reflecting the temperature T and bringing information on the symmetry energy value at the corresponding fragment density ρ_{well} (full blue lines on the figure). Temperatures of the order of $T = 3$ MeV are extracted from the simulations. One can observe that the BLOB calculations become closer to the analytical predictions at the largest time

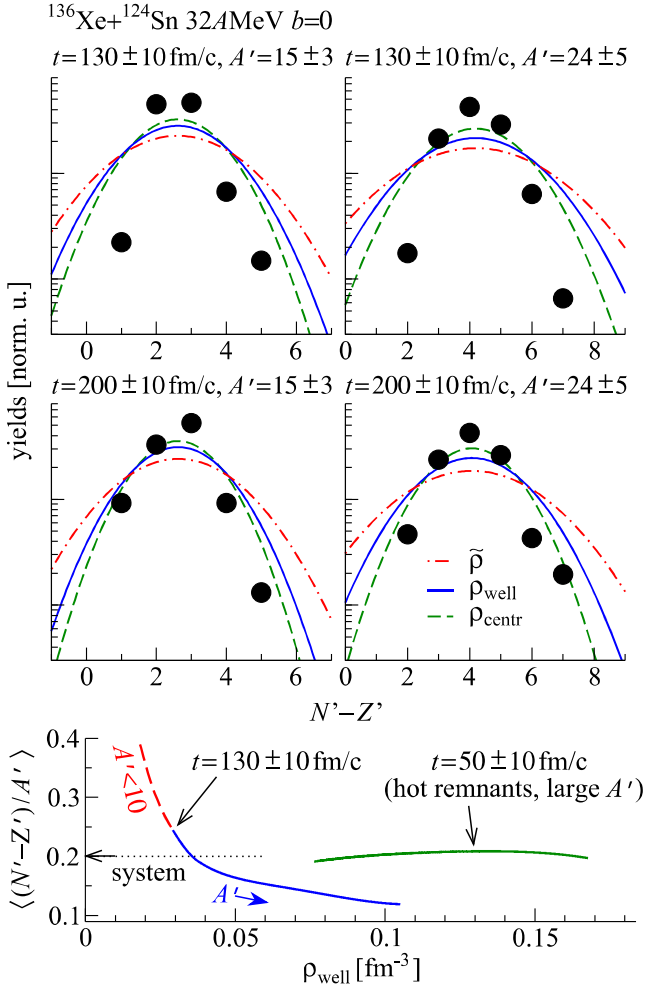


Figure 13: (Color online) BLOB simulation of head-on $^{136}\text{Xe}+^{124}\text{Sn}$ collisions at 32 A MeV. (upper row) Isotopic distribution (full dots) in potential ripples containing N neutrons and Z protons for cluster-forming configurations with masses around $A=15$ (left) and $A=24$ (right) at $t=130$ fm/c. The lines correspond to analytic distributions (see text), corresponding to the density extracted from different portions of potential ripples. (middle row) The same as in the upper row, but at $t=200$ fm/c. (bottom) Average isospin content measured in potential ripples at two different times, as indicated on the figure, as a function of the ripple density ρ_{well} . Larger density values correspond to prefragments of larger mass. The dot-dashed line with an arrow indicates the asymmetry of the projectile-target composite system. Taken from [116].

instant considered, though they remain narrower. This indicates that, whereas the BLOB fluctuation treatment looks efficient in out-of-equilibriums and/or unstable situations, providing the seeds for fragment formation, some refinements are still needed to properly describe the fluctuations characterizing the following (thermodynamical) interaction phase among formed fragments. These fluctuation issues are a crucial point to be checked in transport codes, in order to link fragment isotopic features to the trend of the symmetry energy [126].

4.3 Concluding remarks on multifragmentation

The results reviewed above indicate that the pre-equilibrium and fragmentation dynamics is quite sensitive to the subtle interplay between mean-field and many-body correlation effects. This may lead to different predictions of the transport models which are commonly employed to simulate heavy ion collisions, according to the different approximations adopted to go beyond the mean-field picture. Whereas closer results are obtained for IMF multiplicities and charge distributions, light cluster and isospin observables exhibit a larger sensitivity to the treatment of the many-body dynamics. In particular, one observes that composition and N/Z ratio of the pre-equilibrium emission, as predicted by BUU-like and QMD-like models, can be different. As discussed above in the specific case of the comparison between AMD and SMF models, for a fixed parametrization of the symmetry potential the isotopic content of the emitted light particles appears model-dependent, being systematically lower in SMF, that also gives a more abundant emission. As a consequence, though the IMF charge distributions may exhibit some similarities, IMFs are predicted neutron-richer in SMF than in AMD.

The latter observations lead to the conclusion that isospin observables not only reflect the features

of the isovector channel of the nuclear effective interaction, but they are largely affected by the global reaction dynamics. This could be simply expected from the fact that the symmetry potential is density dependent, however the impact of the nuclear dynamics on these observables looks generally more intricate, also revealing the presence of correlations and clustering effects. One may conclude that the discrepancies between transport model predictions should be ascribed essentially to differences in the description of compression-expansion dynamics and many-body correlations, which affect isoscalar, as well as isovector properties, of the reaction products. From this point of view, isospin observables could be also exploited as a tracer of the reaction dynamics, to probe pre-equilibrium stage and fragmentation path.

Finally, it would be quite appealing to extend the comparison of pre-equilibrium and fragmentation features discussed above to other approaches recently introduced to deal with the nuclear many-body dynamics, namely approaches incorporating explicit light cluster production [76] and new stochastic models [116, 66].

5 Reaction dynamics at medium energy: semi-peripheral collisions

In the previous Section, we focused our attention on multifragmentation processes observed in central collisions at Fermi energies. At semicentral impact parameters, the mechanism changes from fusion/fragmentation to predominant binary channels (which give rise to deep-inelastic or quasi-fission processes); along this transition an intermediate mechanism appears where a low-density neck region, from which fragments can eventually emerge, is produced between projectile-like (PLF) and target-like (TLF) fragments. A qualitative illustration of the mechanism is given in Fig.14.

In addition to volume instabilities, surface effects (and related instabilities) are particularly important for the description of the configuration paths encountered in low- and Fermi-energy heavy ion collisions. As far as the description of low-energy nuclear processes is concerned, it is worth mentioning that stochastic extensions of time-dependent quantum approaches have been recently proposed [54, 127, 55]. Within this scheme, quantum and/or thermal fluctuations are injected in the initial conditions, leading to a spread of dynamical trajectories and corresponding variances of physical observables. Interesting results have been obtained for spontaneous fission of superheavy systems [56]. One could envisage a smooth transition from quantum models to the semi-classical treatments discussed here. In particular, at Fermi energies we still expect thermal and/or mean-field fluctuations to influence dynamical fragment emission from the neck region and from PLF/TLF sources.

The neck fragmentation with a peculiar intermediate mass fragment ($2 < Z < 20$) distribution and an entrance channel memory was observed experimentally and predicted by various transport models [46, 128, 129, 130, 131, 132, 133, 134, 135, 136, 137, 138, 139, 140, 141]. An interplay between statistical and dynamical emission mechanisms can be expected; however it is possible to identify clear dynamical signatures, such as the appearance of hierarchy effects of the IMF size vs. transverse velocity, which keep track of the cluster formation time scale and of the related impact of many-body correlations. Moreover, the analysis of the IMF relative velocities with respect to PLF and TLF reveals that a large fraction of fragments emitted at mid-rapidity cannot be associated with statistical emission from PLF and TLF sources, since they deviate from the Viola systematics [137]. The dynamical nature of these fragments has been probed also through the comparison with transport models. An example is given in Fig.15, which shows the charge distribution of the IMFs emitted at mid-rapidity, for the system $^{124}\text{Sn} + ^{64}\text{Ni}$ at 35 MeV/nucleon. Experimental data [137] are compared to SMF simulations, which predict a prompt dynamical emission. The model is able to reproduce also fragment velocity distributions. The good agreement supports the interpretation of the neck emission in terms of the occurrence of

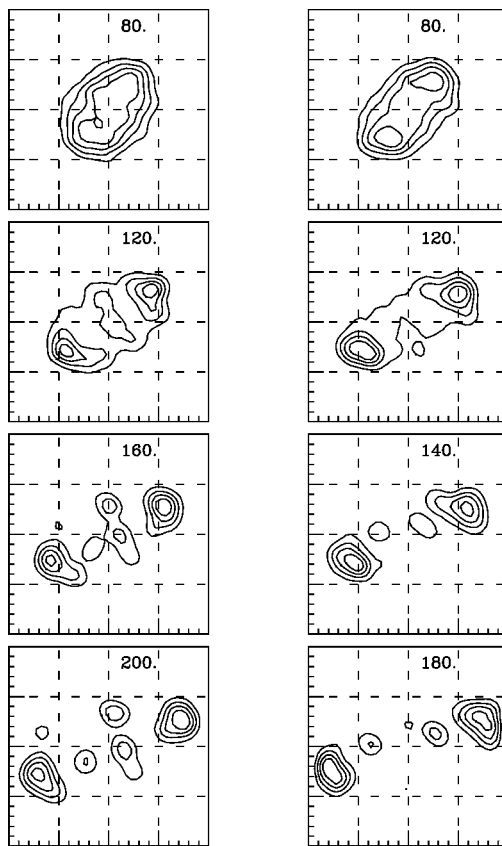


Figure 14: Contour plots of the density projected on the reaction plane, calculated with SMF, for the reaction $^{112}\text{Sn} + ^{112}\text{Sn}$ at 50 MeV/nucleon, at several time instants (fm/c) indicated on the panels. The lines are drawn at projected densities beginning at 0.07 fm^{-2} and increasing by 0.1 fm^{-2} . The size of each box is 40 fm. Left column: impact parameter $b = 4 \text{ fm}$. Right column: $b = 6 \text{ fm}$. Taken from [2].

volume/surface instabilities, according to the scenario offered by given transport models.

Isospin effects are expected also in semi-peripheral reactions. Indeed, the low-density neck region may trigger an isospin migration from the PLF and TLF regions, which have normal density. Therefore, the isospin content of the neck fragments could reflect the isospin enrichment of the mid-velocity region. Moreover, new interesting correlations between fragment kinematical features and isotopic properties, which can provide clues in searching for the most sensitive observables to the symmetry energy, are noted and are still under intense scrutiny.

For more peripheral collisions, the binary mechanism is accompanied, for N/Z-asymmetric entrance channel combinations, by isospin diffusion, that drives the system toward charge equilibration. This mechanism has been widely exploited to probe the low-density behavior of the symmetry energy [142, 4, 143, 144, 145].

In the following we will focus our discussion mainly on isospin dynamics, which has been the object of more recent investigations, and we will review a selection of results related to isospin observables typical of semi-peripheral and peripheral collisions at Fermi energies.

5.1 Isospin transport at Fermi energies

As anticipated above, reactions between charge asymmetric systems are characterized by a direct isospin transport in binary events (isospin diffusion). This process occurs through the low density neck region and thus it is expected to manifest a sensitivity to the low density behavior of C_{sym} , see Refs.[3, 142, 143, 144, 4, 145]. Moreover, it is now quite well established that a large part of the reaction cross section

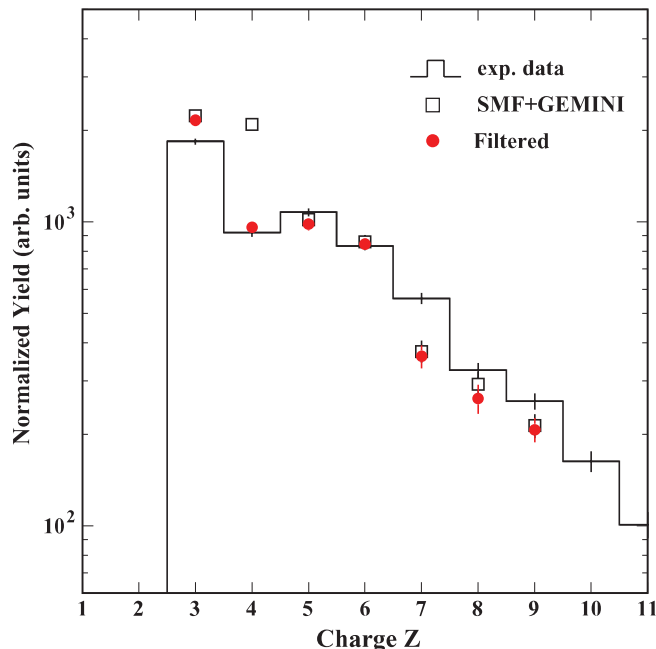


Figure 15: (Color online) Experimental charge distribution of dynamically emitted IMFs detected in the $^{124}\text{Sn} + ^{64}\text{Ni}$ reaction at 35 MeV/nucleon. The squares correspond to the SMF+GEMINI calculations. Red circles: filtered calculated data. The large effect of the detector filter on the charge $Z = 4$ is due to the unbound ^8Be isotope that is present in the calculation, but filtered because it is not identified in the data analysis. Taken from [137].

measured in the Fermi energy range goes into the neck fragmentation channel, with IMFs directly emerging from the interacting zone on short time scales [129, 137]. Fragments are still formed in a dilute asymmetric matter but always in contact with the regions of the projectile-like and target-like remnants, almost at normal densities. This may favor the neutron enrichment of the low-density neck region (isospin migration).

The main role of the isospin degree of freedom in the collision dynamics can be easily understood at the hydrodynamical limit, considering the behavior of neutron and proton chemical potentials as a function of density ρ and asymmetry $\beta \equiv I = \rho_3/\rho$ [146]. The proton/neutron currents can be expressed as

$$\mathbf{j}_{p/n} = D_{p/n}^\rho \nabla \rho - D_{p/n}^\beta \nabla \beta, \quad (31)$$

with $D_{p/n}^\rho$ the drift, and $D_{p/n}^\beta$ the diffusion coefficients for transport dynamics [146]. Of interest for the study of isospin effects are the differences of currents between protons and neutrons which have a simple relation to the density dependence of the symmetry energy

$$\begin{aligned} D_n^\rho - D_p^\rho &\propto 4\beta \frac{\partial C_{sym}}{\partial \rho}, \\ D_n^\beta - D_p^\beta &\propto 4\rho C_{sym}. \end{aligned} \quad (32)$$

From these simple arguments, one can realize that the isospin transport due to density gradients (isospin migration) is ruled by the slope of the symmetry energy, or the symmetry pressure, while the transport due to isospin concentration gradients (isospin diffusion) depends on the symmetry energy value. Hence transport phenomena in nuclear reactions appear directly linked to two relevant properties (direct value and first derivative) of the symmetry energy of the nuclear EOS.

5.1.1 Charge equilibration in peripheral collision dynamics

In semi-peripheral and peripheral reactions, transport simulations allow one to investigate the asymmetries of the various parts of the interacting system in the exit channel: emitted particles, PLF and TLF fragments, and, for ternary (or higher multiplicity) events, IMFs. In particular, one can study the

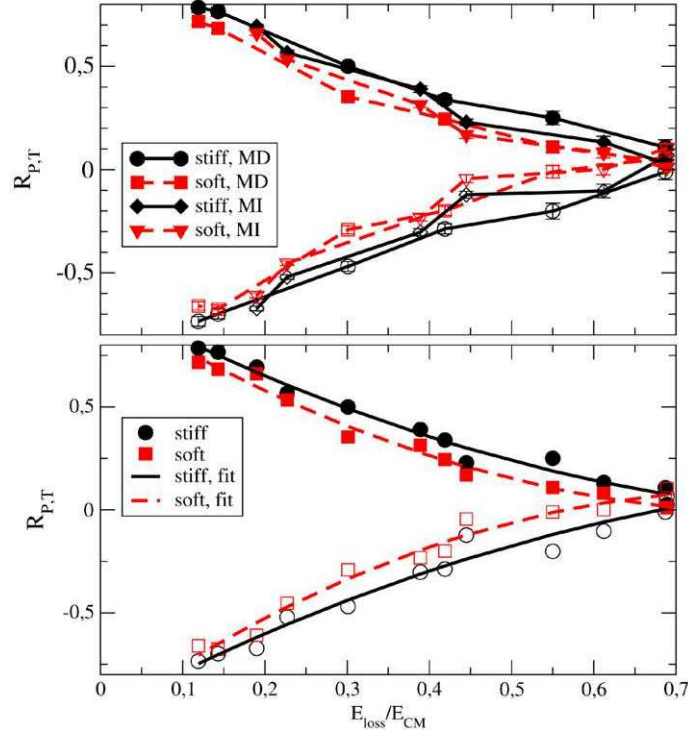


Figure 16: (Color online) Projectile (P, upper curves in each panel) and target (T, lower curves in each panel) imbalance ratio as a function of relative energy loss. Upper panel: separately for stiff (solid) and soft (dashed) asyEOS, and for MD (circles and squares) and MI (diamonds and triangles) interactions, in the projectile region (full symbols) and the target region (open symbols). Lower panel: quadratic fit to all points for the stiff (solid), respectively soft (dashed) asyEOS. Taken from [143].

so-called isospin transport ratio (or imbalance ratio), which is defined as:

$$R_{P,T}^x = \frac{2(x^M - x^{eq})}{(x^H - x^L)}, \quad (33)$$

with $x^{eq} = \frac{1}{2}(x^H + x^L)$. Here, x is an isospin sensitive quantity that has to be investigated with respect to equilibration [147, 3]. One can directly consider the asymmetry $I = (N - Z)/A$, but also other quantities, such as isoscaling coefficients, ratios of light fragment's yields, etc, can be of interest [3, 4, 148, 126]. The indices H and L refer to symmetric reactions between heavy (n -rich) and light (n -poor) systems, while M refers to the mixed reaction. P, T denote the rapidity region, in which this quantity is measured, in particular the PLF and TLF rapidity regions. Clearly, this ratio is ± 1 in the projectile and target regions, respectively, for complete transparency, and oppositely for complete rebound, whereas it is zero for complete equilibration.

The centrality dependence of the isospin transport ratio has been widely explored in experiments as well as in theory [3, 142, 143, 144, 4, 145]. Many investigations have been concentrated on Sn + Sn collisions at 35 and 50 MeV/nucleon [3]. Some examples are given below. Fig.16 shows the results of SMF calculations employing Momentum Dependent (MD) or Momentum Independent (MI) Skyrme interactions [143]. The transport ratio, evaluated considering, as the x observable of Eq.(33), the N/Z

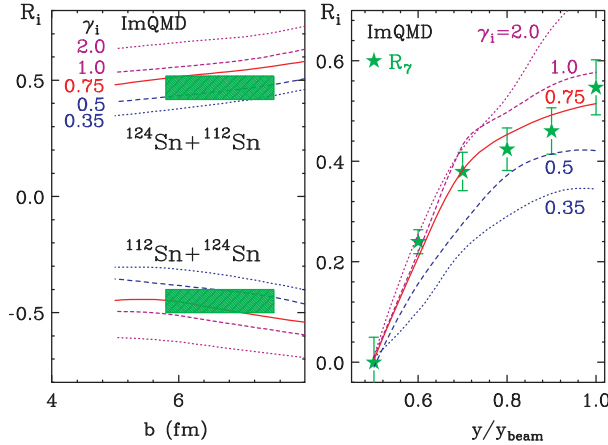


Figure 17: (Color online). Left panel: Comparison of experimental isospin transport ratios (shaded regions) to ImQMD results (lines), as a function of impact parameter for different values of the parameter γ_i , related to the symmetry energy behavior. Right panel: Comparison of experimental isospin transport ratios obtained from the yield ratios of $A = 7$ isotopes (star symbols), as a function of the rapidity, to ImQMD calculations (lines) at $b = 6$ fm. Reprinted from [4], with kind permission of the APS.

ratio of primary PLF and TLF, is reported as a function of the kinetic energy loss. The latter quantity is taken as an estimate of the dissipation degree reached along the collision dynamics and thus of the contact time between the reaction partners. The energy dissipation between projectile and target is mainly governed by the isoscalar features of the nuclear interaction (including effective mass details) [149]. On the other hand, for the same amount of dissipated energy, the sensitivity of the isospin transport ratio to the symmetry energy is nicely isolated (see the lines on the bottom panel of Fig.16). More equilibration, i.e. a smaller R ratio, is obtained in the case of an asysoft parametrization, which is associated with a higher symmetry energy value below normal density (see Fig.3). Quite sizeable isospin equilibration effects characterize the semi-central events (corresponding to large dissipated energy).

Calculations performed with the ImQMD model, together with a thorough comparison to the *MSU* experimental data, are reported in [4]. Corresponding results are shown in Fig.17, for the transport ratio as a function of the impact parameter (left panel) and of the fragment rapidity (right panel). Several parametrizations of the symmetry energy, denoted by the parameter γ_i (see the discussion in Section 3) are employed. The predictions of the SMD and ImQMD models look comparable for peripheral collisions, where a low degree of charge equilibration is observed in both cases, however SMF predicts a larger equilibration at semi-central impact parameters. This can be expected on the basis of the faster dynamics, i.e. the larger transparency characterizing QMD-like models [32], with respect to mean-field ones. We observe again that not only isospin observables hold a sensitivity to the density behavior of the symmetry energy, but they also trace the many-body reaction dynamics.

It is worth noticing that the isospin transport ratio is also affected by isoscalar features of the nuclear effective interaction [143, 149]. Also clustering effects may impact this observable, as pointed out, for instance, in Ref.[61].

The information on the stiffness of the symmetry energy, extracted from the comparison performed in Ref.[4], see Fig.17 (left panel), points to a value of the slope L in the range between 40 and 80 MeV. With respect to the model dependence discussed above, this conclusion should be rather robust because the analysis is performed at semi-peripheral impact parameters, where the predictions of different models are closer to each other.

5.1.2 Neck fragmentation at Fermi energies: isospin dynamics

As discussed above, in presence of density gradients, as the ones occurring when a low-density neck region is formed between the two reaction partners, the isospin transport is mainly ruled by the density derivative of the symmetry energy, see Eqs.(32), and so we expect a larger neutron flow toward the neck clusters for a stiffer symmetry energy around saturation [46] (see Fig.3). As predicted by some

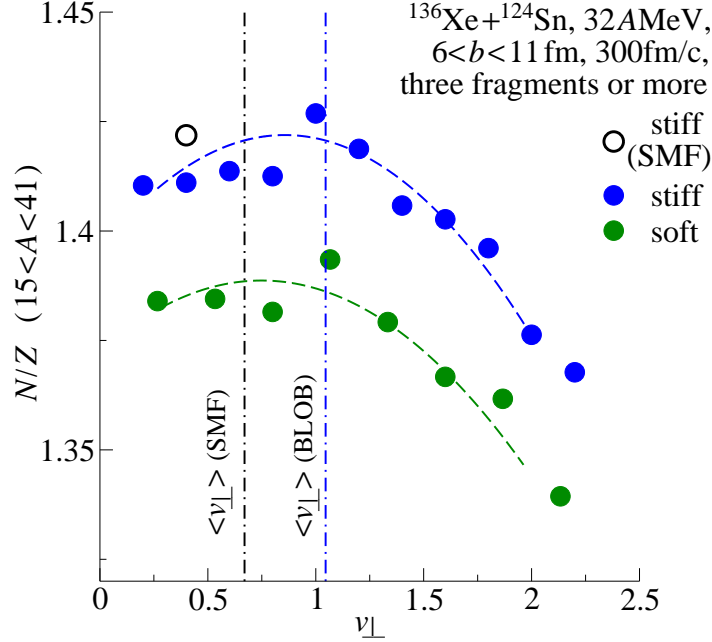


Figure 18: (Color online) BLOB simulations: Isotopic content of neck fragments at 300fm/c, identified in the impact parameter region of maximum production, as a function of the transverse velocity component with respect to the PLF-TLF axis for a stiff and a soft form of the symmetry energy potential. Taken from [120].

transport models, this mechanism (isospin migration) appears as a good candidate to explain the neutron enrichment of the neck region. The effect is illustrated in Fig.18, where the neutron enrichment of the neck primary fragments, simulated with BLOB, is shown as a function of their transverse velocity, for the reaction $^{136}\text{Xe}+^{124}\text{Sn}$ at 32 MeV/A. Two different parametrizations of the nuclear symmetry energy are employed (asystiff and asysoft). Two interesting features emerge from these results: i) the neutron migration effect is larger at smaller transverse velocity, i.e. for fragments which stay for a longer time in contact with the PLF/TLF regions (thus experiencing a more effective isospin migration); ii) neutron-richer fragments are obtained in the asystiff case, confirming the sensitivity of the effect to the symmetry energy derivative. These features, related to primary fragment emission, could be blurred by secondary decay, thus it would be desirable to build observables that should be less affected by the de-excitation stage. A possibility would be to consider ratios of fragment yields or isotopic features. For instance, one can adopt the ratio of the asymmetry of the IMFs (β_{IMF}) to that of the residues (β_{res}). For symmetric projectile/target reactions, this quantity can be roughly estimated analytically on the basis of simple energy balance considerations. By imposing to get a maximum (negative) variation of $C_{sym}(\rho)$ when transferring the neutron richness from PLF and TLF towards the neck region, one obtains [143]:

$$\frac{\beta_{IMF}}{\beta_{res}} = \frac{C_{sym}(\rho_R)}{C_{sym}(\rho_I)} \quad (34)$$

From this simple argument the ratio between IMF and residue (PLF and TLF) asymmetries should depend only on symmetry energy properties and, in particular, on the different symmetry energy values

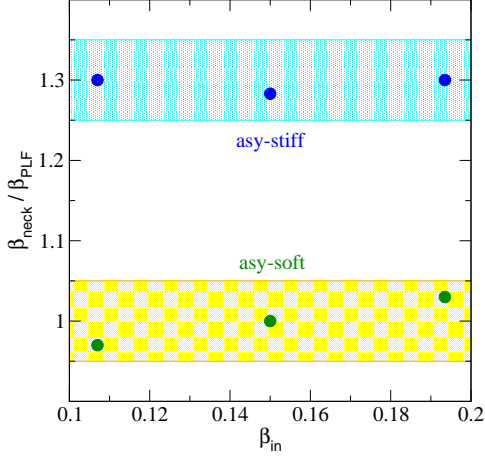


Figure 19: Ratio between the neck IMF and the PLF/TLF asymmetries, in Sn + Sn reactions at 50 $AMeV$, as a function of the system initial asymmetry. SMF simulations. The bands indicate the uncertainty in the calculations. Taken from [48], with kind permission of the European Physical Journal (EPJ).

associated with residue and neck densities (ρ_R and ρ_I , respectively), as appropriate for isospin migration. It should also be larger than one, more so for the asystiff than for the asysoft EOS. Results obtained with SMF, employing the asystiff and asysoft parametrizations (see Fig.3), are represented in Fig.19, for Sn + Sn systems with different initial asymmetry, β_{in} , at 50 MeV/nucleon of beam energy. One can see that this ratio is nicely dependent on the asyEOS only (being larger in the asystiff case) and not on the system considered. Assuming that final asymmetries are affected in a similar way by secondary evaporation, one could directly compare the results of Fig.19 to data. However, some words of caution are needed, because of the different size/temperature conditions of the neck region with respect to PLF and TLF sources.

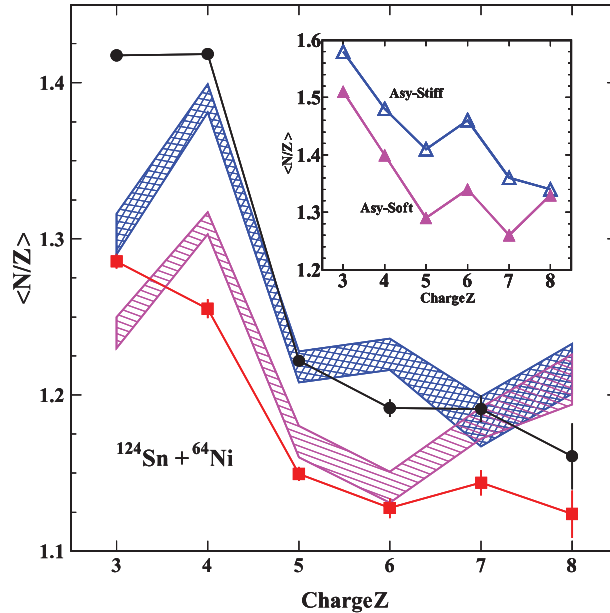


Figure 20: (Color online) Experimental $\langle N/Z \rangle$ distributions, as a function of the charge Z , for statistically emitted (solid squares - red line) and dynamical emitted fragments (solid circles - black line), for the reaction $^{124}\text{Sn} + ^{64}\text{Ni}$. Blue hatched area: SMF-GEMINI calculation for dynamical emitted particles and asystiff parametrization; magenta hatched area: asysoft parametrization. The $\langle N/Z \rangle$ of primary IMFs as a function of the atomic number Z , as obtained in SMF calculations, is plotted in the inset for the two parametrizations. The hatched zone indicates the error bars in the calculations. Taken from [137].

We now move to review some recent experimental evidences related to the neutron enrichment of the neck fragments [137, 150, 140, 141]. The isotopic features of the neck emission have been investigated in experimental analyses performed on Sn+Ni data at 35 $AMeV$ by the Chimera Collab.[137] The experimental observation that these fragments are neutron-rich appears compatible with the isospin migration mechanism predicted by stochastic mean-field models. Provided that charge distribution and kinematical properties of the neck fragments are also consistently described, this observable can probe the density dependence of the symmetry energy, as shown in Fig.20. First of all one can see that, in the data analysis [137], the “dynamical” emission (black line), i.e. the fragments which are directly emitted at mid-rapidity, exhibits a larger N/Z than the “statistical” emission from PLF/TLF sources (red line). SMF simulations, including statistical de-excitation, (the bands on the figure) indicate that an asystiff parametrization of the symmetry energy leads to a better agreement with the data. Within the same data set, a strong correlation between neutron enrichment and fragment alignment (which enforces a short emission time) has been evidenced. The comparison with the simulations point to a stiff behavior of the symmetry energy ($L \approx 75 MeV$). We notice that this result is compatible with the constraints extracted from the analysis of the isospin transport ratio discussed in the previous subsection.

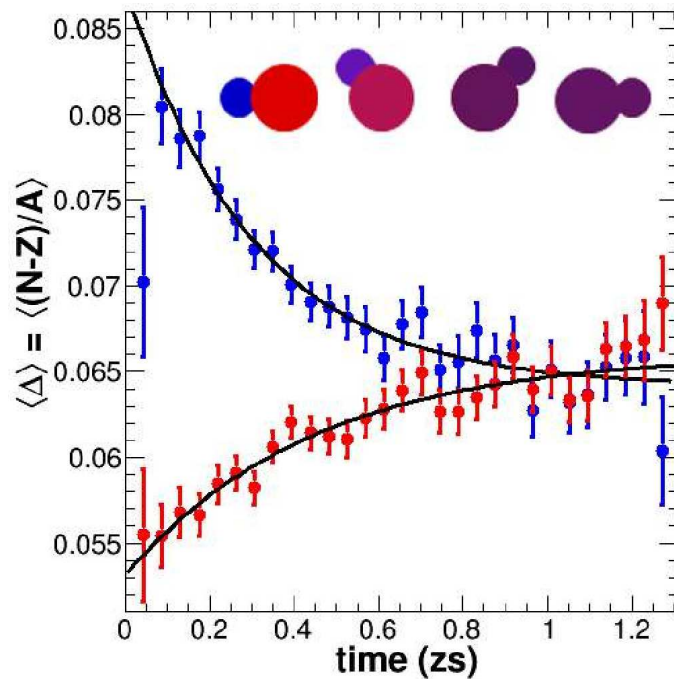


Figure 21: (Color online) Measured neutron excess of both the heavy (red) and light (blue) daughters produced in binary splits of a deformed excited projectile-like fragment as a function of the duration of the equilibration. Data shown is for $^{70}\text{Zn} + ^{70}\text{Zn}$ at 35 MeV/u, $Z_H = 12$, $Z_L = 7$. The cartoon across the top suggests the neutron-rich (blue) - proton-rich (red) equilibration as the system rotates. Taken from [151].

New experimental studies have been devoted to probe the isotopic content of the fragments emitted at mid-rapidity, in connection to kinematical features and emission time scales [140, 141]. In particular, the main goal was to explore the interplay between the isospin migration/diffusion effect and the time scales characterizing the fragment emission dynamics. Fig.21 illustrates the features of the two fragments (of charge Z_L and Z_H) emitted on short time scales from deformed PLF sources, in semi-peripheral reactions at typical Fermi energies. Emission times are extracted from the light fragment emission angle, according to the estimated PLF intrinsic angular momentum. It is seen that the light fragments are neutron-richer when their orientation with respect to the (heavier) projectile-like fragment corresponds to a small angle, i.e. they are promptly emitted, along a rather aligned configuration. The

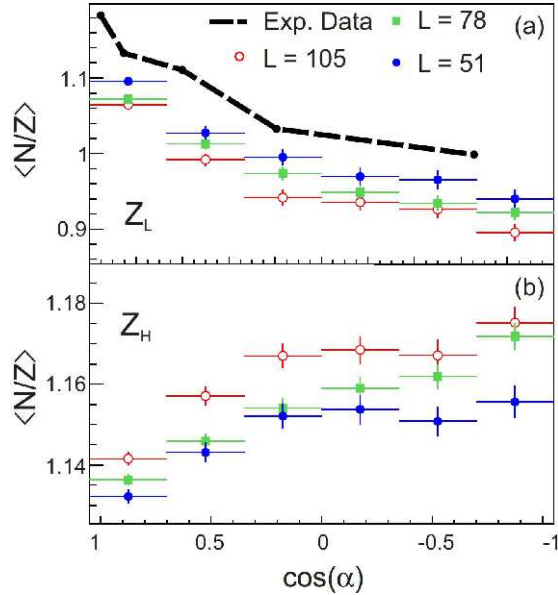


Figure 22: (Color online) Top panel: Composition of the light fragment as a function of its orientation relative to the projectile-like fragment for reactions of Zn+Zn at 45 MeV/u. Black: measured data. Color points: CoMD model calculations for varying forms of the asymmetry energy. Bottom panel: The CoMD model also shows how the composition of the heavy fragment changes in proportion and in the opposite direction to the composition of the light fragment. Reprinted from [152], with kind permission of the APS.

latter observation would be consistent with the fact that the light fragments, when promptly emitted, still reflect the neutron enrichment of the neck region. On the other hand, larger emission angles would correspond to a longer emission time, i.e. to a significant rotation of the light fragment around the heavy one, that would lead to isospin equilibration, prior to the emission, among the two objects. This would correspond to an increase (decrease) of the N/Z of the light (heavy) fragment, towards equilibration.

In Fig.22 the experimental data are compared to the results of the CoMD model [37]. It is interesting to see that the model is able to reproduce the decreasing (increasing) trend of the N/Z of the light (heavy) fragment with the emission time, i.e. the emission angle. The calculations also exhibit a sensitivity to the symmetry energy parametrization employed (denoted by the slope parameter L on the figure). However, the model predicts neutron-richer heavy fragments, with respect to the light ones (compare top and bottom panels), contrarily to what is observed in the data, see Fig.21, and expected on the basis of isospin migration arguments. A deeper discussion about the predictions of different transport models is tackled in the next subsection.

5.2 Comparison between the predictions of different transport models

A closer inspection of the main mechanisms governing energy dissipation and isospin transport can be made by comparing the predictions of different transport models. As shown by Figs.16 and 17, which illustrate charge equilibration for $Sn + Sn$ reactions at 50 MeV/nucleon, for the most central reactions the ImQMD code predicts a quite different behavior with respect to SMF: indeed the trend of the isospin transport ratio versus the impact parameter is flatter in ImQMD. This behavior would suggest that, even in the case of central collisions, the contact time between the two reaction partners remains rather short, inhibiting charge equilibration. Then energy dissipation is mainly due to nucleon correlations and particle emission, rather than to mean-field effects. In other words, the faster (and more explosive) dynamics predicted by ImQMD simulations would lead to the lower degree of isospin equilibration

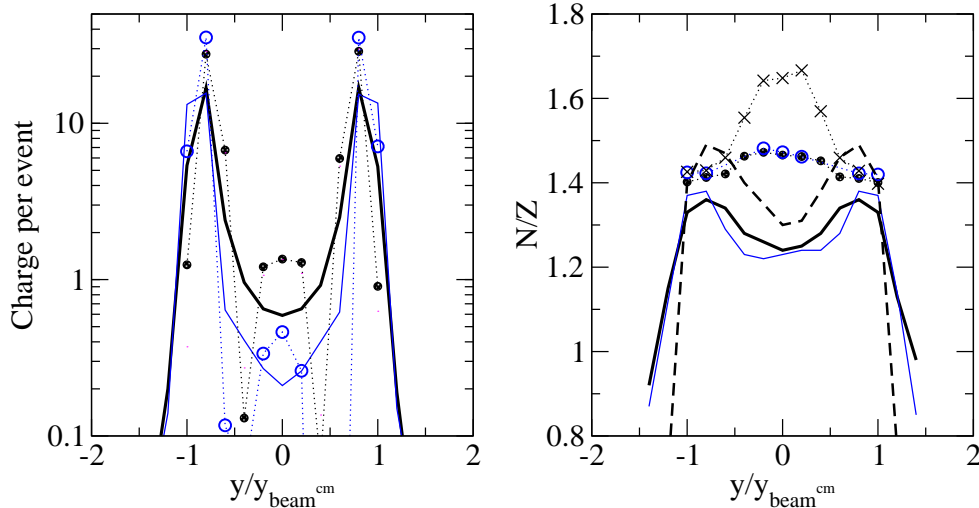


Figure 23: (Color online) Left panel: Average total charge per event, associated with IMFs, as a function of the reduced rapidity, obtained in the reaction $^{124}\text{Sn} + ^{124}\text{Sn}$ at 50 MeV/u. Results are shown for ImQMD calculations at $b = 6$ fm (thick black line) and $b = 8$ fm (thin blue line) and for SMF calculations at $b = 6$ fm (full circles) and $b = 8$ fm (open circles). A soft interaction is considered for the symmetry energy. Right panel: N/Z of IMFs as a function of the reduced rapidity. Lines and symbols are like in the left panel. Results corresponding to a stiff asyEOS are also shown for ImQMD (dashed line) and SMF (crosses), for $b=6$ fm. Taken from [48], with kind permission of the European Physical Journal (EPJ).

observed. It should be noticed that the stronger impact, in molecular dynamics approaches, of many-body correlations on the fragmentation path was evidenced also in the case of central multifragmentation reactions, see the discussion concerning the comparison between AMD and SMF approaches in Section 4.2 [43].

To explore in deeper details the neck fragmentation dynamics, results concerning IMF ($Z > 2$) properties, obtained with the SMF and ImQMD codes, are compared in Fig.23. In the left panel, the average total charge per event, bound in IMFs, is plotted as a function of the reduced rapidity, for the reaction $^{124}\text{Sn} + ^{124}\text{Sn}$ at 50 MeV/u and impact parameters $b = 6$ and 8 fm. It appears that in ImQMD a larger number of light IMFs, distributed over all the rapidity range between PLF and TLF, are produced. On the other hand, mostly binary or ternary events are observed in SMF, with light IMFs located very close to mid-rapidity. These observations are consistent with the results obtained for charge equilibration, especially in semi-peripheral reactions ($b \approx 4-6$ fm). In fact, a more abundant cluster production goes in the direction of reducing isospin equilibration, as also discussed in Ref.[61] in the context of the pBUU model. The fast ImQMD fragmentation dynamics inhibits nucleon exchange and charge equilibration, though the energy loss can be sizeable, owing to particle and light cluster emission. On the other hand, in the SMF model, mean-field effects, acting over longer time intervals, have a stronger impact on dissipation, leading to more equilibration.

Results on the fragment neutron content are illustrated in the right panel of Fig.23, that shows the global N/Z of IMFs as a function of the reduced rapidity. As already discussed above, SMF calculations clearly predict a larger N/Z for IMFs produced at mid-rapidity, with respect to PLF and TLF regions (isospin migration). The effect is particularly pronounced in the case of the asystiff parametrization. On the contrary, ImQMD calculations predict a minimum of the N/Z ratio at mid-rapidity, probably caused by the abundant neutron emission from the hotter neck region, suggesting that isospin migration toward the neck is not present. We notice that the observation of mid-velocity (light) fragments with smaller or comparable N/Z with respect to the heavier ones, is consistent with the CoMD results presented in

Fig.22. Interestingly enough, isospin migration effects towards IMFs at mid-rapidity are absent also in pBUU calculations including explicit cluster correlations, whereas standard BUU simulations (i.e. without clusters) predict it [61]. In perspective, it would be interesting to investigate isospin transport effects also in the recently upgraded AMD model, including explicit cluster production [76]. From the above discussions it emerges that, in addition to the expected sensitivity to the symmetry energy, isospin diffusion and, to an even larger extent, isospin migration are quite affected by the treatment of many-body dynamics. From the experimental point of view, it would be interesting to study both isospin transport phenomena (isospin equilibration and migration) within the same data set[153]. This should allow to further probe, through the comparison with transport simulations, the underlying reaction mechanisms and validate the current constraints on the symmetry energy trend at sub-normal density.

6 Collision dynamics at relativistic energies

For beam energies in the range of 0.1 - 1 GeV/nucleon, the heavy ion reaction dynamics is characterized by a larger degree of stopping in central collisions [73], with also high density and temperatures values explored, which may lead to the full disassembly of the system into nucleons and light clusters. Cluster and IMF production holds also at semi-central/peripheral impact parameters, together with the detection of some remnants of PLF and TLF fragments. Nuclear collisions in this energy range are the ideal tool to investigate the relationship between pressure, density and temperature characterizing the EOS of dense nuclear matter. We stress again that the latter is a rather important object, which also governs the compression achieved in supernovae and neutron stars, as well as their internal structure. The pressure that results from the high densities reached during collisions at relativistic energies strongly influences the motion of the ejected matter. Thus sensitive observables can be devised to probe the high density EOS [1].

Also in this energy regime, the collective response of the system deserves strong attention. Collective flows are very good candidates to probe the reaction dynamics since they are expected to be quite sensitive to the features of the nuclear effective interaction, including the momentum dependence of the mean field, see [154, 46]. On the other hand, stopping observables look more sensitive to the details of the in-medium n-n cross section [1, 73].

The transverse flow, $V_1(y, p_t) = \langle \frac{p_x}{p_t} \rangle$, where $p_t = \sqrt{p_x^2 + p_y^2}$ is the transverse momentum and y the rapidity along the beam direction, provides information on the anisotropy of nucleon (or particle) emission on the reaction plane. Very important for the reaction dynamics is also the elliptic flow, $V_2(y, p_t) = \langle \frac{p_x^2 - p_y^2}{p_t^2} \rangle$. The sign of V_2 indicates the azimuthal anisotropy of the emission: on the reaction plane ($V_2 > 0$) or out-of-plane (*squeeze - out*, $V_2 < 0$).

The flow mechanisms, and their dependence on the nuclear EOS, can be qualitatively explained as it follows: After the initial compression phase, the spectator nucleons (i.e. the nucleons which remain outside the overlap area) initially block the escape of the compressed region along trajectories in the reaction plane, thus forcing the matter to flow in directions perpendicular to the reaction plane. At a later stage, after these spectator nucleons have moved away, the particles from the squeezed central region preferentially escape along trajectories on the reaction plane, which are no longer blocked. The in-plane emission becomes dominant at higher incident energies (about 5 GeV/nucleon), because the spectator nucleons move quickly away. Thus, along the reaction path, nucleon emission first occurs out of plane, then spreads into all directions in the transverse plane and finally it favors the reaction plane. It is clear that this evolution mainly reflects the interplay between the time scale associated with the blockage induced by the spectator matter and the time scale related to the pressure and corresponding flow of the compressed matter, the latter being directly connected to the EOS. In fact, a more repulsive mean field potential leads to higher pressures and to a quicker expansion flow, with the spectator matter still present around. On the other hand, a softer mean field generates a slower expansion and

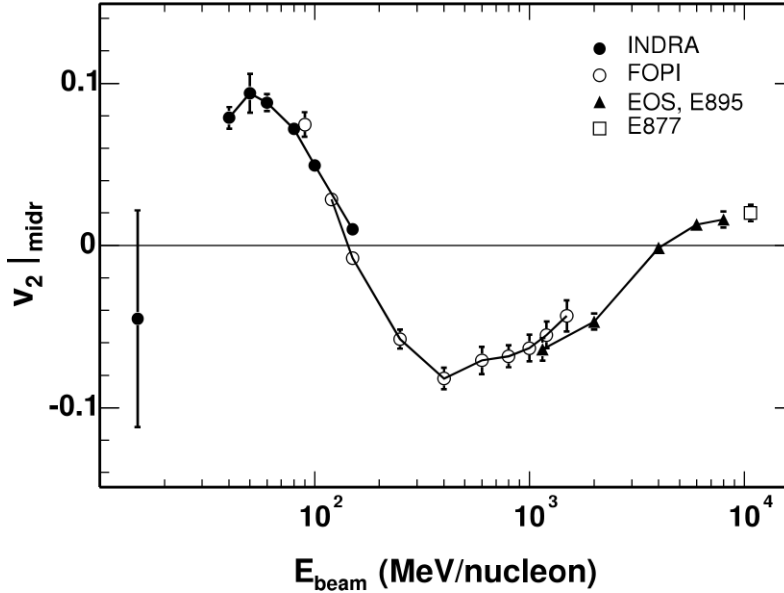


Figure 24: Elliptic flow parameter v_2 at mid-rapidity for $^{197}\text{Au}+^{197}\text{Au}$ collisions at intermediate impact parameters ($b = 5.5\text{-}7.5$ fm), as a function of incident energy. The filled and open circles represent the INDRA and FOPI data for $Z = 1$ particles, the triangles represent the EOS and E895 data for protons, and the squares represent the E877 data for all charged particles. Figure reprinted from [155], with kind permission of the European Physical Journal (EPJ), where the references to the data are also given.

preferential emission on the reaction plane, after the spectators have passed. The sideways deflection or transverse flow of the spectator fragments (the v_1 observable) is mainly generated by the pressure exerted from the compressed region on the spectator matter and it is positive at relativistic energies. It acquires negative values for reactions at beam energies below the so-called balance energy (around 50 MeV/nucleon), because of the dominance of attractive mean-field effects.

On the other hand, the elliptic flow reflects the blockage of the spectators on the participant zone.

A systematics of elliptic flow measurements, for Au + Au collisions at intermediate impact parameters, is shown in Fig.24, as a function of the beam energy. It is interesting to see how the elliptic flow evolves from positive values (observed at beam energies up to 100 MeV/nucleon), indicating that particle emission occurs mainly in plane because of the moderate pressure effects, to negative values (up to energies of the order of 1 GeV/nucleon), corresponding to out-of-plane emission. As expected on the basis of the arguments presented above, the elliptic flow becomes positive again at high energy (beyond 1 GeV/nucleon) [155, 156, 157, 158]

In the beam energy interval under consideration, the flow observables reflect the behavior of the EOS at the central densities, in the range of 2 to 5 ρ_0 predicted by transport model simulations. From a thorough analysis of transverse and elliptic flows, based on the comparison between model predictions and experimental data, robust constraints on the nuclear matter compressibility have been derived [1], pointing to a value between 200 and 300 MeV.

From the discussion above, it is clear that reactions at relativistic energies (0.1-1 GeV/nucleon) allow one to generate high momentum particles and to probe regions of high baryon and (in the case of neutron-rich systems) isovector density during the reaction dynamics. In the theoretical description of these collisions, the momentum dependence of the nuclear effective interactions, leading to isoscalar effective mass and neutron/proton effective mass splitting, is rather important. The problem of the precise determination of the momentum dependence in the isovector channel of the nuclear interaction [159, 160] is still controversial and it would be extremely important to get more definite experimental information, looking at observables which may also be sensitive to the mass splitting, see Ref.[161] for

a recent review.

6.1 Collective flows and isospin effects

Several investigations, based on both BUU-like and QMD-like models, have focused on particle emission and collective dynamics characterizing heavy ion reactions at incident energy around 0.5 GeV/nucleon. One of the goals of these analyses was to constrain the symmetry energy behavior at supra-saturation densities. In particular, the difference between neutron and proton flows, that is mainly ruled by the balance between the Coulomb repulsion (acting for protons) and the symmetry potential (repulsive for neutrons in neutron-rich systems), appears as a suitable observable to probe the isovector channel of the nuclear effective interaction [162, 163, 164, 165].

Transport codes are usually implemented with different (n, p) density and momentum dependent interactions, see for instance [159, 160]. This allows one to probe different symmetry energy parametrizations and also to follow the dynamical effect of opposite n/p effective mass (m^*) splitting while keeping the same symmetry energy behavior [143, 102].

As an example, we discuss below some results obtained for semicentral ($b/b_{max}=0.5$) collisions of $^{197}\text{Au}+^{197}\text{Au}$ at 400 MeV/nucleon. Transport models predict that in the interacting zone baryon densities around $1.7 - 1.8\rho_0$ can be reached in a transient time of the order of 15-20 fm/c. The system is quickly expanding and the freeze-out time is around 50 fm/c. A rather abundant particle emission is observed over this time scale [162, 165]. Figure 25, represents the elliptic flow of emitted neutrons

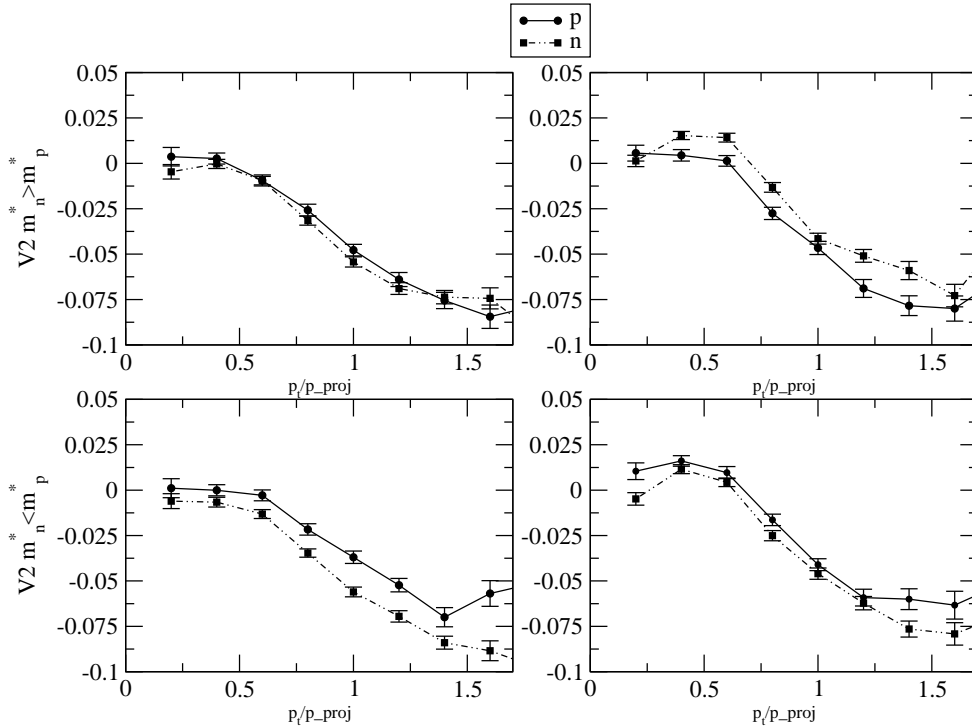


Figure 25: Proton (thick) and neutron (thin) V_2 flows in a semi-central reaction Au+Au at 400 $AMeV$. Transverse momentum dependence for particles emitted at mid-rapidity, $|y_0| < 0.3$. Upper curves for $m_n^* > m_p^*$, lower curves for the opposite splitting $m_n^* < m_p^*$. Left: asystiff. Right: asysoft. Taken from [165].

and protons, as obtained in BUU-like calculations [165], for different asy-stiffness and effective mass splitting choices. We are now exploring density regions above normal density, thus we expect a larger neutron repulsion in the asystiff case, corresponding to the larger symmetry energy value (see figure

3). Indeed Fig.25 shows that a larger (negative) neutron v_2 , close or even larger than the proton v_2 , is obtained in the asystiff case (compare left and right panels). Moreover, one can see that the $m_n^* < m_p^*$ case favors the neutron repulsion, leading to a larger squeeze-out for neutrons (compare top and bottom panels). In particular, in the asysoft case (right panels) we observe an inversion of the neutron/proton squeeze-out trend when using the $m_n^* > m_p^*$ parametrization or considering the $m_n^* < m_p^*$ splitting.

We conclude that a rather interesting interplay exists between the effects linked to symmetry energy and effective mass splitting: a larger (smaller) neutron effective mass may compensate the larger (smaller) neutron repulsion corresponding to the asystiff (asysoft) case. In fact, the $m_n^* < m_p^*$ case, with the asysoft EOS, yields very similar results of the $m_p^* < m_n^*$ case with the asystiff EOS.

This interplay between the effects of several ingredients of the nuclear effective interaction needs to be further investigated [161]. The $m_p^* < m_n^*$ option seems supported by optical model analyses [95].

Reaction dynamics at relativistic energies and collective flows have been analyzed also in QMD-like models (TuQMD and UrQMD codes, [163, 164, 166]), employing different parametrizations of the symmetry energy (asysoft or asystiff, identified by the exponent γ), and a fixed effective mass splitting option (of the $m_p^* \leq m_n^*$ type). The calculated ratio of neutron and proton flows is displayed in Fig.26, where also the ASY-EOS experimental data are plotted [163] (see [10] and references therein).

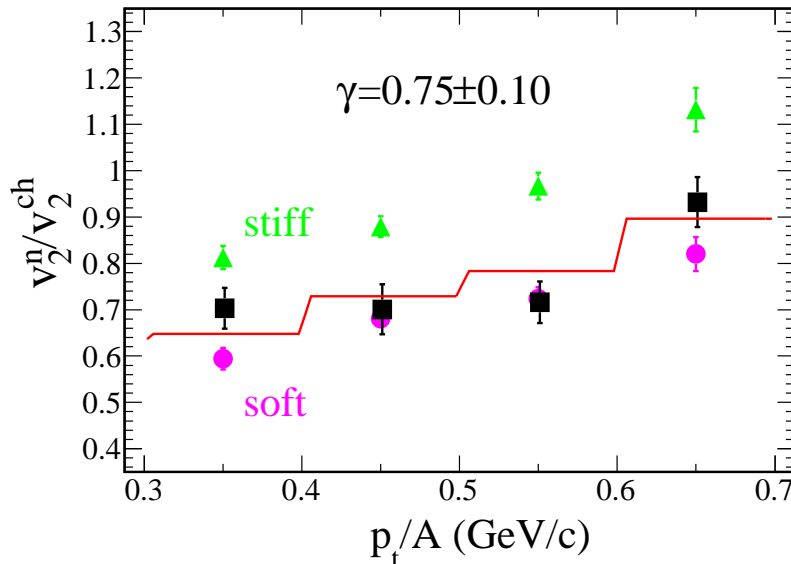


Figure 26: (Color online) Elliptic flow ratio of neutrons over all charged particles for central ($b < 7.5$ fm) collisions of $^{197}\text{Au}+^{197}\text{Au}$ at 400 MeV/nucleon, as a function of the transverse momentum per nucleon p_t/A . The black squares represent the experimental data, the green triangles and purple circles represent the UrQMD predictions for stiff ($\gamma = 1.5$) and soft ($\gamma = 0.5$) power-law exponents of the potential symmetry term, respectively. The solid line is the result of a linear interpolation between the predictions, weighted according to the experimental errors, and leading to the indicated $\gamma = 0.75 \pm 0.10$. Taken from [10].

The latter analysis has recently allowed to extract new constraints, emerging from high density dynamics, on the symmetry energy slope: $L = 72 \pm 13$ MeV. A global picture of the symmetry energy behavior, obtained combining the results discussed above and the low-density constraints deriving from reaction mechanisms at Fermi energies and structure effects is given in Fig.27. In particular, the low-density behavior represented in the figure is evinced from the isospin diffusion analysis discussed in Section 5.1.1 [4] and from constraints associated with the energy of the Isobaric Analog State (IAS) in several nuclei [167]. The black points correspond to constraints coming from structure properties (ground state features of doubly magic nuclei [168] and neutron skin thickness of heavy nuclei [169]).

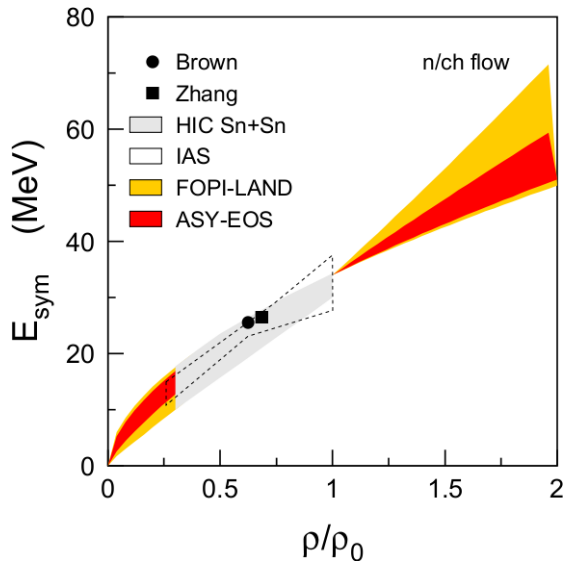


Figure 27: (Color online) Constraints deduced for the density dependence of the symmetry energy from the ASY-EOS data [10] in comparison with the FOPI-LAND result of Ref.[163], as a function of the reduced density ρ/ρ_0 . The low-density results of Refs.[4, 167, 168, 169] are given by the symbols, the grey area (Heavy Ion Collisions), and the dashed contour (IAS). For clarity, the FOPI-LAND and ASY-EOS results are not displayed in the interval $0.3 < \rho/\rho_0 < 1.0$. Taken from [10].

New analyses, aimed at probing symmetry energy and effective mass splitting at once, could possibly couple the flow information to the study of other observables in heavy ion reactions. For instance, the N/Z content of particle emission looks more sensitive just to the sign of the effective mass splitting, rather than to the asy-stiffness [165], as also observed for the energetic particles emitted in reactions at Fermi energies [160, 102], see Section 4.1.1. It would be interesting the combine observables related to particle flows and yields. Recent experimental analyses look very promising in this direction [10]. Owing to the difficulties in measuring neutrons, one could also consider the difference between light isobar (like ${}^3\text{H}$ vs. ${}^3\text{He}$) flows and yields. We still expect to observe symmetry energy and effective mass splitting effects [165]. It should also be noticed that, as already discussed for reactions at Fermi energies, the treatment of cluster correlations could have a significant impact on the nucleon and light particle observables discussed here.

6.2 Meson production

A quite interesting observable to probe both reaction dynamics and isospin effects is meson production, arising from inelastic n-n collisions. In particular, processes related to n-n scattering strongly depend on the energy and density conditions reached during the initial compression phase and, as such, bear precious information on the nuclear EOS. Indeed, kaon production has been one of the most useful observables to determine the EOS of symmetric nuclear matter [170]. Turning to isospin effects, isotopic meson ratios, such as the pion π^-/π^+ ratio, are expected to reflect the N/Z content of the high density regions explored along the reaction dynamics, which is connected to the symmetry energy behavior [162, 9]. A simple explanation of this relation is as it follows: The isovector channel of the nuclear interaction is responsible for the different forces felt by neutrons and protons in the medium. This difference has an impact on the N/Z content of the nucleons that escape from the system and, consequently, of the matter which remains kept inside the interacting nuclear system and may increment particle production through inelastic n-n scattering. For instance, pions are produced predominantly via the Δ resonances $NN \rightarrow N\Delta$ and the subsequent decay $\Delta \rightarrow N\pi$. The ratio of the isospin partners π^-/π^+ can thus

serve as a probe of the high-density symmetry energy.

An illustration of this effect is given in Fig.28, which represents the results of BUU calculations for $^{197}\text{Au} + ^{197}\text{Au}$ collisions, see Ref.[9]. One observes that a larger π^-/π^+ ratio is obtained for the soft parametrization of the symmetry energy. In this case, owing to the lower neutron repulsion at high density, see Fig.3, the interacting nuclear system remains neutron-richer, thus favoring π^- production. More recent calculations, performed with Relativist BUU (RBUU) or QMD codes, have shown that

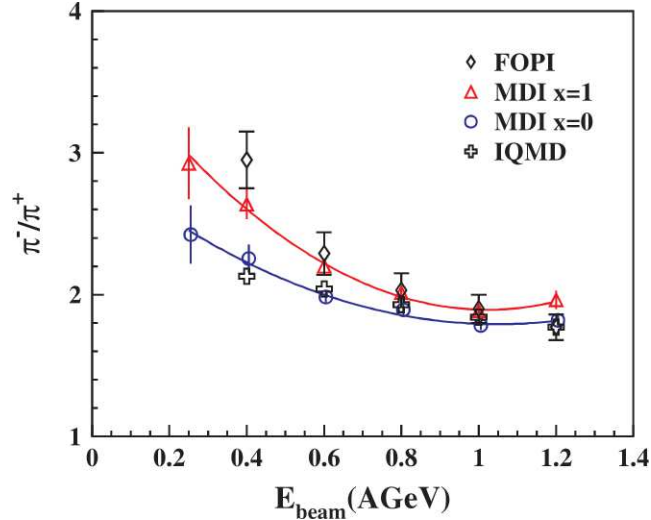


Figure 28: (Color online) Excitation function of the π ratio in the most central Au + Au collisions. A soft symmetry energy corresponds to the parameter $x = 1$ (red line), whereas $x = 0$ denotes a stiff parametrization (blue line). Reprinted from [9], with kind permission of the APS.

emission threshold effects, which act differently for π^+ and π^- , may reverse the trend of the pion ratio, with respect to the effects discussed just above [171, 172, 173]. This can be illustrated within the relativistic framework introduced in Section 2.7. The “threshold effect” stems from the fact that nucleon and Δ masses are modified in the medium. The unknown self-energies of the Δ s are usually specified in terms of the neutron and proton ones by the use of Clebsch-Gordan coefficients for the isospin coupling of the Δ s to nucleons [174, 175]. These in-medium modifications are isospin dependent and they influence the phase-space available for meson production in a n-n collision, because the difference between the invariant energy in the entrance channel s_{in} and the production threshold s_{th} changes. This effect is, of course, present in general for all meson production, but, just for the sake of illustration, we consider here one specific inelastic channel: $nn \rightarrow p\Delta^-$, mainly responsible for π^- production. According to Eqs.(26), the invariant energy in the entrance channel and the threshold energy are given, respectively, by

$$\sqrt{s_{in}}/2 = [E_n^* + \Sigma^0] \rightarrow_{p \rightarrow 0} [m_N^* + \Sigma_\omega^0 + \Sigma_\rho^0 + \Sigma_\delta] > m_N^* + \Sigma_\omega^0 \quad (35)$$

$$\sqrt{s_{th}} = [m_p^* + m_{\Delta^-}^* + \Sigma_p^0 + \Sigma^0(\Delta^-)] = [m_N^* + m_\Delta^* + 2\Sigma_\omega^0] \quad (36)$$

where m_N , m_Δ are the isospin averaged values for nucleon and Δ masses. The last equality for the threshold energy derives from the prescription for the Δ self-energies, which leads to an exact compensation of the isospin-dependent parts, thus the threshold s_{th} is not modified by the isospin dependent self-energies. In general, in a self-consistent many-body calculation higher order effects can destroy this exact balance, however compensating effects are expected anyway in s_{th} . On the other hand, the energy available in the entrance channel, s_{in} , is shifted in an explicitly isospin dependent way by the in-medium self-energy $\Sigma_\rho^0 + \Sigma_\delta > 0$. In particular, the vector self-energy gives a positive contribution to neutrons that increases the difference $s_{in} - s_{th}$, thus enlarging the cross section of the inelastic process, owing to the opening up of the phase-space. This happens especially close to the

production threshold, since the intermediate Δ resonance will be better probed. A similar modification but opposite in sign is present in $s_{in} - s_{th}$ for the $pp \rightarrow n\Delta^{++}$ channel that therefore is suppressed by the isospin effect on the self-energies. In conclusion, owing just to threshold effects, the ratio π^-/π^+ is predicted to increase with the stiffness of the symmetry energy C_{sym} ; indeed a stiffer trend leads to a larger $(\Sigma_\rho^0 + \Sigma_\delta)$ self energy.

RBUU calculations contain isospin contributions also in the mean field propagation, but the results look dominated by the threshold effect discussed above, in particular at lower energies [171].

Threshold effects on pion production are illustrated in Fig.29, which reports the results of RBUU calculations employing $NL\rho$ and $NL\rho - \delta$ models [173]. Calculations are compared to the FOPI data [176]. On the left panel, one can observe that neglecting threshold effects the pion ratio is larger in the softer $NL\rho$ case, in agreement with the BUU calculations discussed above [9]. On the other hand, the trend is reversed when threshold effects are turned on. Indeed in the latter case a larger pion ratio is obtained for the $NL\rho - \delta$ parametrization, which corresponds to a stiffer symmetry energy [171, 173]. The right panel shows calculations that include threshold effects and also a density-dependent production cross section. In this case a good reproduction of the experimental data can be obtained not only for the pion ratio (shown on the figure), but also for the separate π^- and π^+ yields [173]. A

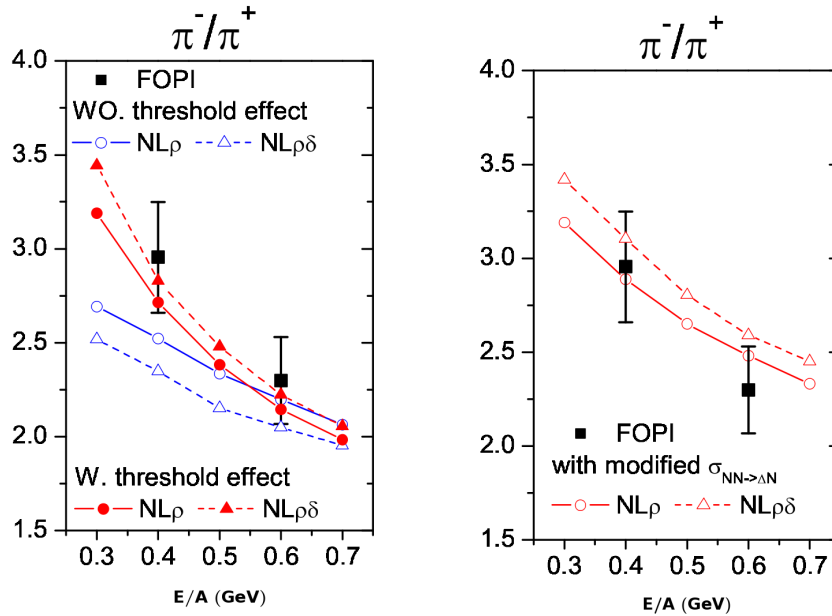


Figure 29: Left panel: π^-/π^+ ratio as a function of the collision energy with and without the threshold effect in Au+Au collisions at impact parameter of 1.4 fm from the $NL\rho$ and $NL\rho - \delta$ models. Experimental data are from the FOPI Collaboration [176]. Right panel: π^-/π^+ ratio as a function of the collision energy obtained with the threshold effect and the density-dependent production cross section in Au+Au collisions at impact parameter of 1 fm for both the $NL\rho$ and $NL\rho - \delta$ models. Adapted from [173], with kind permission of the APS.

further illustration of the importance of effects related to the threshold mechanism, namely global energy conservation (GEC) in inelastic n-n collisions, is provided below, in the context of QMD-like calculations [172]. Fig.30 reports the pion ratio, obtained in central Au + Au collisions at 400 MeV/nucleon, as a function of the parameter x which identifies the stiffness of the symmetry energy parametrization employed, ranging from negative (stiffer) to positive (softer) values. Comparing the GEC results to the other options, one can nicely see that enforcing energy conservation leads to a reversal of the trend of

the pion ratio with respect to the symmetry energy stiffness. The figure also shows the effects induced by in-medium modification of the production cross section.

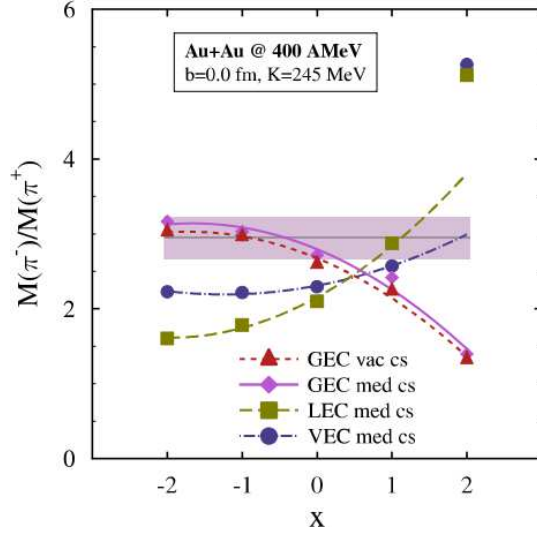


Figure 30: The π^-/π^+ ratio for the vacuum (vac cs) and in-medium (med cs) cross-sections scenarios for the case of global energy conservation (GEC) as a function of the asyEOS stiffness parameter x . Results for the LEC and VEC approximations making use of in-medium modified cross-sections (“med cs”) are also displayed. The experimental FOPI results [176] are represented by horizontal bands. Taken from [172].

As far as threshold effects are concerned, some other physical aspects should be considered. One is the fact that the self-energies usually employed in relativistic calculations are not explicitly momentum dependent, as studies of the optical potential would require. Thus we come back to the importance of the isospin momentum dependence already discussed for collective flows (see previous subsection). Because we neglect the dependence of the self-energies on momentum, the difference $s_{in} - s_{th}$ might increase too strongly with the energy, i.e. the temperature of the composite nuclear system. It is likely that a more realistic calculation, including such a momentum dependence, would reduce the threshold effects discussed above. In addition, a fully consistent treatment should include an optical potential also for the pions. More generally, open problems in pion production include the treatment of the width of the Δ resonance (off-shell effects), the density dependence of the Δ production cross section in the medium and the pion potentials in the nuclear medium [177, 178, 179, 180, 181]. The latter effect, i.e. the inclusion of the pion potential, seems to go in the direction of smaller pion ratios. A global representation of threshold and pion potential effects is given in Fig.31, which display RBUU results [180]. Adopting the $NL\rho$ interaction (corresponding to a symmetry energy slope $L = 83$ MeV), one observes that the charged pion ratio is increased by threshold (Th) effects, reduced by s-wave pion potential (S), increased by p-wave pion potential (P), finally acquiring a slightly larger value (green point, Th + S + P) than obtained without any in-medium effects. A good reproduction of the FOPI data would require to employ a parametrization with a smaller symmetry energy slope parameter $L \approx 60$ MeV. We notice that the latter would be comparable to the constrained values extracted from nuclear structure and reactions studies discussed above.

Other interesting effects on pion production are related to many-body dynamics. Indeed, as already noted, reactions at relativistic energies are characterized by a huge amount of light cluster emission. One may expect an interplay between clustering effects and meson production. Recent AMD calculations, including cluster correlations, have shown that light cluster emission affects the pion ratios [182]. This is illustrated in Fig.32, which reports results obtained for central $^{132}\text{Sn}+^{124}\text{Sn}$ collisions at 300 MeV/nucleon. Several isospin ratios are plotted on the figure. The different lines correspond to AMD

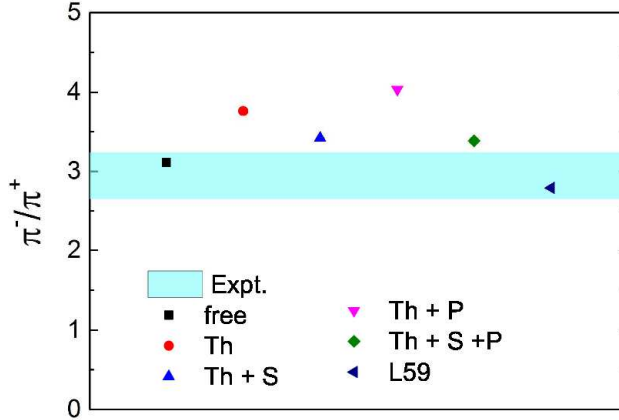


Figure 31: (Color online) The π^-/π^+ ratio in Au + Au collisions at impact parameter of 1.4 fm and energy of $E/A = 400$ MeV from the $NL\rho$ model in different cases (see text for details). Experimental data [176] from the FOPI collaboration are shown as the cyan band. Reprinted from [180], with kind permission of the APS.

calculations with or without cluster correlations, for a soft or a stiff parametrization of the symmetry energy, and to a cascade calculation (JAM, black line). One can see that, especially in the asystiff case, the inclusion of cluster correlations has a significant impact on the final pion ratios. Larger ratios are obtained, reflecting the larger N/Z of the high density phase (see in particular the high-momentum nucleons), when clustering effects are turned on. This could be ascribed to the fact that the produced light clusters are mainly symmetric, thus the N/Z of the nucleons which experience inelastic collisions and may produce pions increase. There is presently an intense activity in the field of meson production, also triggered by new devoted experiments [183]. It can be envisaged that a stronger sensitivity to the features of the effective interaction and, in particular, to the symmetry energy, can be seen looking at pion ratios as a function of the transverse energy.

It has also been suggested that the ratio of the anti-strange kaon isospin partners, K^0/K^+ , could be a useful observable to probe the symmetry energy behavior above normal density. Indeed kaons weakly interact with nuclear matter and thus could keep a direct signature of the properties of the dense matter in which they are produced [171].

7 Conclusions and perspectives

In this article, we have reviewed recent results connected to the rich phenomenology offered by heavy ion collisions, from medium up to relativistic energies. Transport theories are essential to tackle the description of the collision dynamics and to connect the features of the nuclear effective interaction (and nuclear EOS) to the predictions of reaction observables which can be directly compared to experimental data. In particular, our discussion was focused on the subtle interplay between mean-field dynamics and many-body correlations in determining the reaction path, and on isospin effects. We have shown that theoretical investigations can allow one to scrutinize the complex nuclear many-body dynamics and, at the same time, to learn about fundamental nuclear matter properties, of great interest also in the astrophysical context.

Selected observables and corresponding constraints which have been extracted over the past years were reviewed. For reactions at Fermi energies, our attention has been focused on the mechanisms responsible for light particle and fragment emission. Several isospin transport effects, such as “isospin migration” and charge equilibration, have been discussed. Whereas the charge distribution of the reaction products emerging from central reactions provides information on the nuclear matter com-

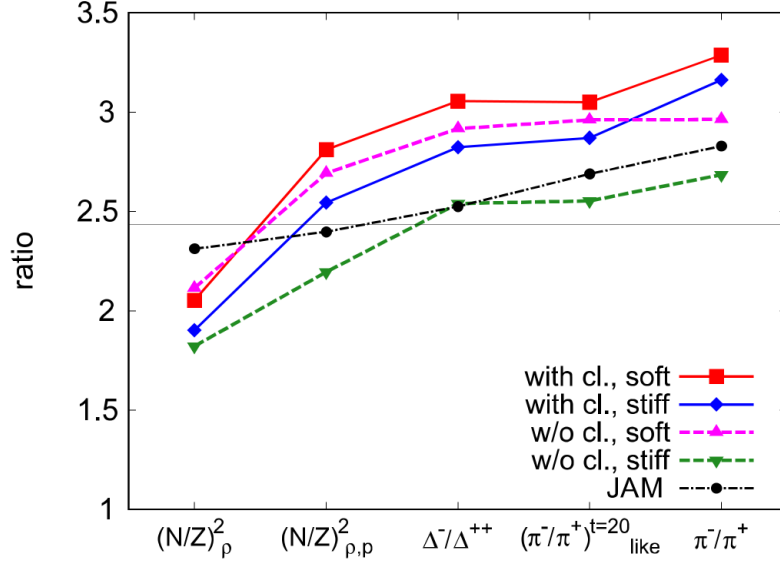


Figure 32: The nucleon ratios $(N/Z)_\rho^2$ and $(N/Z)_{\rho,p}^2$ in the high-density region with and without high-momentum condition, respectively, the Δ^-/Δ^{++} production ratio, the pion-like ratio at $t = 20$ fm/c, and the final π^-/π^+ ratio (see Ref.[182] for more details). Each line connects the ratios for each of the five cases of calculation for central collisions of $^{132}\text{Sn}+^{124}\text{Sn}$ at 300 MeV/nucleon. The horizontal line represents the $(N/Z)_{sys}^2$ ratio of the total system. The statistical uncertainties in the final π^-/π^+ ratio are smaller than 0.03. Reprinted from [182], with kind permission of the APS.

pressibility and on the role of many-body correlations (like clustering effects), observables connected to isospin transport give constraints on the low-density behavior of the symmetry energy, but also probe the reaction dynamics. At relativistic energies, the collision dynamics is dominated by nucleon and light cluster emission, with a persistence of collective effects, such as transverse flow (for the spectator matter) and elliptic flow. Meson production, arising from inelastic n-n collisions, also sets in. In this regime, neutron/proton collective flows and isotopic meson ratios can constrain the high density behavior of the symmetry energy.

In perspective, it would be highly desirable to reduce the model dependence which presently affects the evaluation of some observables. In particular, the differences between BUU-like and QMD-like approaches need to be understood and accounted for. A dedicated program, aiming at comparing the predictions of different transport models under controlled situations, to understand and eliminate possible sources of discrepancies, is presently running. Some clues have already emerged, concerning the impact of the Pauli principle preservation along the dynamical evolution [185], the robustness of some reaction observables [184] and the description of the inelastic processes generating pion production [186].

Also, it would be quite helpful to investigate several transport observables at the same time, both within the same code and between different codes and different models. The global reaction dynamics could be probed looking at suitable isoscalar observables such as fragment and particle yields and energy spectra, as well as at the isotopic features of the reaction products (and related observables). In particular, the study of pre-equilibrium emission, which is not influenced by secondary decay effects, could prove particularly useful in this direction. More generally, it would be very interesting to explore a consistent map of many observables in a multiparameter physics input space, see for instance the recent Bayesian analysis of Ref.[187].

Finally, to improve our understanding of nuclear dynamics and our knowledge of the nuclear EOS,

the synergy between theory and experiments is of paramount importance. From the experimental point of view, new detection systems and analyses, which allow to investigate several reaction mechanisms and observables within the same data set, look extremely promising.

8 Acknowledgements

Useful discussions with P.Napolitani and H.H.Wolter are gratefully acknowledged. This project has received funding from the European Union's Horizon 2020 research and innovation programme under grant agreement N. 654002.

References

- [1] P. Danielewicz, R. Lacey and W.G. Lynch, *Science* 298 (2002) 1592
- [2] V. Baran, M. Colonna, M. Di Toro *et al.*, *Nucl. Phys. A* 703 (2002) 603
- [3] M.B. Tsang *et al.*, *Phys. Rev. Lett.* 92 (2004) 062701 ; B-A Li, L-W Chen, *Phys. Rev. C* 72 (2005) 064611
- [4] M.B. Tsang *et al.*, *Phys. Rev. Lett.* 102 (2009) 122701
- [5] X.Roca-Maza, N.Paar, *Progress in Particle and Nuclear Physics* 101 (2018) 96 , and refs. therein
- [6] J.M. Lattimer and M. Prakash, *Phys. Rep.* 442 (2007) 109
- [7] S. Burrello *et al.*, *Phys. Rev. C* 92 (2015) 055804
- [8] C.J. Horowitz *et al.*, *Jou. Phys. G* 41 (2014) 093001
- [9] Z. Xiao *et al.*, *Phys. Rev. Lett.* 102 (2009) 062502
- [10] P. Russotto *et al.*, *Phys. Rev. C* 94 (2016) 034608
- [11] M. Baldo, G.F. Burgio, *Progress in Particle and Nuclear Physics* 91 (2016) 203
- [12] S.Hudan *et al.*, *Phys. Rev. C* 67 (2003) 064613
- [13] W. Reisdorf, D. Best, A. Gobbi, N. Herrmann, K. Hildenbrand, B. Hong, S. Jeong, Y. Leifels, C. Pinkenburg, J. Ritman, *et al.*, *Nucl. Phys. A* 612 (34) (1997) 493
- [14] W. Reisdorf, A. Andronic, R. Averbeck, M. Benabderrahmane, O. Hartmann, N. Herrmann, K. Hildenbrand, T. Kang, Y. Kim, M. Kis, *et al.*, *Nucl. Phys. A* 848 (34) (2010) 366
- [15] J. W. Negele and D. Vautherin, *Phys. Rev. C* 5 (1972) 1472
- [16] J. Dechargé and D. Gogny, *Phys. Rev. C* 21 (1980) 1568
- [17] J.R. Stone and P.-G. Reinhard, *Progress in Particle and Nuclear Physics* 58 (2007) 587 , and refs. therein
- [18] M. Bender, P.-H. Heenen, and P.-G. Reinhard, *Rev. Mod. Phys.* 75 (2003) 121 , and refs. therein
- [19] R.Botet *et al.*, *Phys. Rev. Lett.* 86 (2001) 3514
- [20] J.B.Elliott *et al.*, *Phys. Rev. Lett.* 88 (2002) 042701
- [21] M.D'Agostino *et al.*, *Nucl. Phys. A* 699 (2002) 795
- [22] G.Tabacaru *et al.*, *Eur.Phys.Jou.A* 18 (2003) 103
- [23] P. Chomaz, M. Colonna and J. Randrup, *Phys. Rep.* 389 (2004) 263 , and references therein
- [24] A. Ono, *Phys. Rev. C* 59 (1999) 853
- [25] S. Typel, H. H. Wolter, G. Roepke *et al.*, *Eur. Phys. J.A* 50 (2014) 17
- [26] S. Reddy, G. F. Bertsch, and M. Prakash, *Phys. Lett. B* 475 (2000) 1
- [27] J. Margueron, J. Navarro, and P. Blottiau, *Phys. Rev. C* 70 (2004) 028801

- [28] C.J. Horowitz, D.K. Berry, C.M. Briggs *et al.*, *Phys. Rev. Lett.* 114 (2015) 031102
- [29] G. F. Bertsch, S. D. Gupta, A guide to microscopic models for intermediate energy heavy ion collisions, *Phys. Rep.* 160 (4) (1988) 189
- [30] A. Bonasera, F. Gulminelli and J. Molitoris, *Phys. Rep.* 243 (1994) 1
- [31] Jun Xu, *Progress in Particle and Nuclear Physics* 106 (2019) 312
- [32] J. Aichelin, *Phys. Rep.* 202 (1991) 233
- [33] H. Feldmeier, Fermionic molecular dynamics, *Nucl. Phys. A* 515 (1) (1990) 147
- [34] M. Colonna and Ph. Chomaz, *Phys. Lett. B* 436 (1998) 1
- [35] A. Ono, H. Horiuchi, T. Maruyama, A. Ohnishi, Antisymmetrized version of molecular dynamics with two-nucleon collisions and its application to heavy ion reactions, *Progress of theoretical physics* 87 (5) (1992) 1185
- [36] A. Ono, H. Horiuchi, T. Maruyama, A. Ohnishi, Fragment formation studied with antisymmetrized version of molecular dynamics with two-nucleon collisions, *Phys. Rev. Lett.* 68 (19) (1992) 2898
- [37] M. Papa *et al.*, *Phys. Rev. C* 64 (2001) 024612
- [38] Y. Zhang and Z. Li, *Phys. Rev. C* 74 (2006) 014602
- [39] S. Ayik, C. Gregoire, *Phys. Lett. B* 212 (1988) 269 ; S. Ayik and C. Gregoire, NPA 513 (1990) 187
- [40] Y. Abe, S. Ayik, P.-G. Reinhard and E. Suraud, *Phys. Rep.* 275 (1996) 49
- [41] J. Randrup and B. Remaud, *Nucl. Phys. A* 514 (1990) 339
- [42] Y. Kanada-En'yo, M. Kimura, A. Ono, Antisymmetrized molecular dynamics and its applications to cluster phenomena, *Progress of Theoretical and Experimental Physics* (2012) 01A202
- [43] M. Colonna, A. Ono and J. Rizzo, *Phys. Rev. C* 82 (2010) 054613
- [44] B.D. Serot, J.D. Walecka, *Int. J. Mod. Phys. E* 6 (1997) 515
- [45] S. Typel and H.H. Wolter, *Nucl. Phys. A* 656 (1999) 331
- [46] V. Baran, M. Colonna, V. Greco and M. Di Toro, *Phys. Rep.* 410 (2005) 335
- [47] B.A. Li, L.W. Chen and C.M. Ko, *Phys. Rep.* 465 (2008) 113
- [48] M. Colonna, V. Baran and M. Di Toro, Theoretical predictions of experimental observables sensitive to the symmetry energy, *Eur. Jou. Phys. A* 50, No.2 (2014) 30 , Societa Italiana di Fisica / Springer-Verlag 2014.
- [49] S.-J. Wang, W. Cassing, Explicit treatment of N-body correlations within a density-matrix formalism, *Annals of physics* 159 (2) (1985) 328
- [50] P.-G. Reinhard, and E. Suraud, Stochastic TDHF and the Boltzman-Langevin Equation, *Ann. of Physics* 216 (1992) 98
- [51] C.Y. Wong, and H.H.K. Tang, Extended Time-Dependent Hartree-Fock Approximation with Particle Collisions, *Phys. Rev. Lett.* 40 (1978) 1070
- [52] C.Y. Wong, and H.H.K. Tang, Dynamics of nuclear fluid. V. Extended time-dependent Hartree-Fock approximation illuminates the approach to thermal equilibrium, *Phys. Rev. C* 20 (1979) 1419
- [53] D. Lacroix, S. Ayik, et Ph. Chomaz, Nuclear collective vibrations in extended mean-field theory, *Progress in Particle and Nuclear Physics* 52 (2004) 497
- [54] D. Lacroix *et al.*, *Eur. Phys. Jou. A* 52 (2016) 94
- [55] C. Simenel, *Eur. Phys. Jou. A* 48 (2012) 152
- [56] Y. Tanimura, D. Lacroix, S. Ayik, *Phys. Rev. Lett.* 118 (2017) 152501
- [57] P. Danielewicz, Quantum theory of nonequilibrium processes, I, *Annals of Physics* 152 (2) (1984) 239

- [58] W. Botermans, R. Malfliet, Quantum transport theory of nuclear matter, *Phys. Rep.* 198 (3) (1990) 115
- [59] O. Buss, T. Gaitanos, K. Gallmeister, H. Van Hees, M. Kaskulov, O. Lalakulich, A. Larionov, T. Leitner, J. Weil, U. Mosel, Transport-theoretical description of nuclear reactions, *Phys. Rep.* 512 (1-2) (2012) 1
- [60] P. Danielewicz, Hadronic transport models, *Acta Phys. Pol.B* 33 (2002) 45
- [61] D.D.S. Coupland *et al.*, *Phys. Rev. C* 84 (2011) 054603
- [62] C. Y. Wong, *Phys. Rev. C* 25 (1982) 1460
- [63] P.Napolitani, M.Colonna and M. Di Prima, *Phys. Conf. Ser.* 515 (2014) 012014
- [64] P. Napolitani, M. Colonna, *Phys. Lett. B* 726 (2013) 382
- [65] J. Rizzo, Ph. Chomaz, M. Colonna, *Nucl. Phys. A* 806 (2008) 40
- [66] Hao Lin and Pawel Danielewicz, *Phys. Rev. C* 99 (2019) 024612
- [67] P.Napolitani and M.Colonna, *EPJ Web of Conferences* 31 (2012) 00027
- [68] Ph.Chomaz, M.Colonna, A.Guarnera and J.Randrup, *Phys. Rev. Lett.* 73 (1994) 3512
- [69] W.J. Xie, J. Su, J. L. Zhu, FS Zhang, F-S Zhang, *Phys. Lett. B* 718 (2013) 1510
- [70] M. Colonna *et al.*, *Nucl. Phys. A* 642 (1998) 449
- [71] A. Ono, S. Hudan, A. Chbihi, J. Frankland, Compatibility of localized wave packets and un-restricted single particle dynamics for cluster formation in nuclear collisions, *Physical Review C* 66 (1) (2002) 014603.
- [72] A. Ono, H. Horiuchi, Antisymmetrized molecular dynamics for heavy ion collisions, *Progress in Particle and Nuclear Physics* 53 (2) (2004) 501
- [73] A.Ono, *Progress in Particle and Nuclear Physics* 105 (2019) 139 , and references therein.
- [74] A. Ono, H. Horiuchi, T. Maruyama, Nucleon flow and fragment flow in heavy ion reactions, *Physical Review C* 48 (6) (1993) 2946
- [75] A. Ono, Cluster correlations in multifragmentation, *Journal of Physics: Conference Series* 420 (2013) 012103
- [76] A.Ono, *Il Nuovo Cimento C* 39 (2016) 390
- [77] P. Danielewicz, G. F. Bertsch, Production of deuterons and pions in a transport model of energetic heavy-ion reactions, *Nucl. Phys. A* 533 (4) (1991) 712
- [78] P. Danielewicz, Q. Pan, Blast of light fragments from central heavy-ion collisions, *Phys. Rev. C* 46 (5) (1992) 2002
- [79] J.D.Walecka, *Ann.Phys.(N.Y.)* 83 (1974) 491
- [80] B.D.Serot, J.D.Walecka in *Advances in Nuclear Physics* Vol. 16, Eds. J.M.Negele and E.Vogt, Plenum, New York, 1986
- [81] M.M.Sharma, M.A.Nagarajan and P.Ring, *Ann.Phys.(NY)* 231 (1994) 110, G.A.Lalazissis, M.M.Sharma, P.Ring and Y.K.Gambhir, *Nucl. Phys. A* 608 (1996) 202
- [82] P.Ring, *Prog.Part.Nucl.Phys.* 37 (1996) 193
- [83] H.Müller, B.D.Serot, *Phys.Rev. C* 52 (1995) 2072
- [84] Z.Y.Ma , N.Van Giai, A.Wandelt, D.Vretenar and P.Ring, *Nucl.Phys. A* 686 (2001) 173, and refs. therein.
- [85] V.Greco, M.Colonna, M.Di Toro, F.Matera, *Phys.Rev. C* 67 (2003) 015203
- [86] B.Blättel, V.Koch and U.Mosel, *Rep.Prog.Phys.* 56 (1993) 1
- [87] C.M.Ko and G.Q.Li, *Jou. of Phys.* G22 (1996) 1673

- [88] V.Greco, M.Colonna, M.Di Toro, G.Fabbri, F.Matera, *Phys.Rev. C* 64 (2001) 045203
- [89] J.Boguta and C.E.Price, *Nucl.Phys. A*505 (1989) 123
- [90] S.R.de Groot, W.A. van Lee and Ch.G. van Weert, *Relativistic Kinetic Theory*, North-Holland Amsterdam 1980
- [91] R.Hakim, *Nuovo Cimento* 6 (1978) 1
- [92] A.Dellafore and F.Matera, *Phys.Rev. C*44 (1991) 2456
- [93] Ad. R. Raduta *et al.*, *Eur. Phys. Jou. A* 50 (2014) 24
- [94] H.Zheng *et al.*, *Phys. Rev. C* 98 (2018) 024622
- [95] Xiao-Hua Li *et al.*, *Phys. Lett. B* 743 (2015) 408
- [96] X. Roca-Maza *et al.*, *Phys. Rev. C* 87 (2013) 034301
- [97] L .G. Cao, G. Colò, H. Sagawa, *Phys. Rev. C* 81 (2010) 044302 ; *Phys. Rev. C* 72 (2005) 067303 ; *Phys. Lett. B* 455 (1999) 25
- [98] R. B. Wiringa, V. Fiks, and A. Fabrocini, *Phys. Rev. C* 38 (1988) 1010
- [99] H.Zheng *et al.*, *Phys. Lett. B* 769 (2017) 424
- [100] H.Zheng *et al.*, *Phys. Rev. C* 94 (2016) 014313
- [101] S.Burrello *et al.*, *Phys. Rev. C* 99 (2019) 054314
- [102] Yingxun Zhang, M.B.Tsang, Zhuxia Li, Hang Liu, *Physics Letters B* 732 (2014) 186190
- [103] J.Margueron, R.Hoffmann Casali, F.Gulminelli, *Phys. Rev. C* 97 (2) (2018) 025805
- [104] F.de Jong, H.Lenske, *Phys.Rev. C*57 (1998) 3099
- [105] F.Hofmann, C.M.Keil, H.Lenske, *Phys.Rev. C*64 (2001) 034314
- [106] B.Borderie and M-F Rivet, *Progress in Particle and Nuclear Physics* 61 (2008) 551
- [107] B.Borderie *et al.*, *Phys. Lett. B* 782 (2018) 291
- [108] B.Borderie and J.D.Frankland, *Progress in Particle and Nuclear Physics* 105 (2019) 82 , and references therein.
- [109] E.Bonnet *et al.*, *Phys. Rev. C* 89 (2014) 034608
- [110] P. Napolitani, M. Colonna, *Eur. Phys. Jou. A* 117 (2016) 07008
- [111] J.B.Natowitz *et al.*, *Phys. Rev. Lett.* 104 (2010) 202501
- [112] D.D.S. Coupland *et al.*, *Phys. Rev. C* 94 (2016) 011601
- [113] M. Colonna and Ph. Chomaz, *Phys. Rev. C* 49 (1994) 1908
- [114] J.D. Frankland, B. Borderie, M. Colonna *et al.*, *Nucl. Phys. A* 689 (2001) 940
- [115] K.Zbiri *et al.*, *Phys. Rev. C* 75 (2007) 034612
- [116] P.Napolitani and M.Colonna, *Phys. Rev. C* 96 (2017) 054609
- [117] D. Durand, *Nucl. Phys. A* 541 (1992) 226
- [118] F. Gagnon-Moisan *et al.* (INDRA Collaboration), *Phys. Rev. C* 86 (2012) 044617
- [119] G. Ademard *et al.* (INDRA Collaboration), *Eur. Phys. Jou. A* 50 (2014) 33
- [120] M. Colonna, P. Napolitani, V. Baran, *Nuclear Particle Correlations and Cluster Physics*, pag.403, Ed. W-U Schroeder, World Scientific, Singapore (2017).
- [121] P.Napolitani and M.Colonna, *Phys. Lett. B* 797 (2019) 134833
- [122] H.S.Xu *et al.*, *Phys. Rev. Lett.* 85 (2000) 716
- [123] M.Colonna, M.Di Toro, A.B.Larionov, *Phys. Lett. B* 428 (1998) 1
- [124] Z.Kohley and S.J.Yennello, *Eur. Phys. Jou. A* 50 (2014) 31
- [125] A.Ono *et al.*, *Phys. Rev. C* 70 (2004) 041604

- [126] M. Colonna, *Phys. Rev. Lett.* 110 (2013) 042701
- [127] D. Lacroix, S. Ayik, B. Yilmaz, *Phys. Rev. C* 85 (2012) 041602
- [128] R. Lioni, V. Baran, M. Colonna and M. Di Toro, *Phys. Rev. C* 71 (2005) 044602
- [129] M. Di Toro, A. Olmi and R. Roy, *Eur. Phys. J. A* 30 (2006) 65 , and refs. therein.
- [130] B. Djerroud *et al.*, *Phys. Rev. C* 64 (2001) 034603 ; J. Colin *et al.* (INDRA Coll.), *Phys. Rev. C* 67 (2003) 064603 ; A.A. Stefanini *et al.*, *Z. Phys. A* 351 (1995) 167
- [131] M. Veselsky *et al.*, *Phys. Rev. C* 62 (2000) 041605(R)
- [132] R.T. de Souza, W.U. Schroeder, J.R. Huizenga, R. Planeta, K. Kwiatkowski, V.E. Viola, and H. Breuer, *Phys. Rev. C* 37 (1988) 1783(R)
- [133] C. P. Montoya *et al.*, *Phys. Rev. Lett.* 73 (1994) 3070
- [134] S.Barlini *et al.*, *Phys. Rev. C* 87 (2013) 054607
- [135] *Phys. Lett. B* 509 (2001) 204
- [136] Z. Kohley *et al.*, *Phys. Rev. C* 83 (2011) 044601
- [137] E. De Filippo *et al.* (Chimera Collab.), *Phys. Rev. C* 86 (2012) 014610
- [138] V. Baran, M. Colonna, M. Di Toro, and R. Zus, *Phys. Rev. C* 85 (2012) 054611
- [139] C. Rizzo, M. Colonna, V. Baran, and M. Di Toro *Phys. Rev. C* 90 (2014) 054618
- [140] A. Jedele *et al.*, *Phys. Rev. Lett.* 118 (2017) 062501
- [141] A. Rodriguez Manso *et al.*, *Phys. Rev. C* 95 (2017) 044604
- [142] L-W Chen, C-M Ko and B-A Li, *Phys. Rev. Lett.* 94 (2005) 032701
- [143] J. Rizzo, M. Colonna, V. Baran, M. Di Toro, H.H. Wolter, M. Zielinska-Pfabe, *Nucl. Phys. A* 806 (2008) 79
- [144] E. Galichet *et al.*, *Phys. Rev. C* 79 (2009) 064615
- [145] Z.Y. Sun *et al.*, *Phys. Rev. C* 82 (2010) 051603
- [146] V. Baran *et al.*, *Phys. Rev. C* 72 (2005) 064620
- [147] F. Rami *et al.*, *Phys. Rev. Lett.* 84 (2000) 1120
- [148] M. Colonna *et al.*, *Phys. Rev. C* 78 (2008) 064618
- [149] Y. Zhang, M. B. Tsang, and Z. Li, *Phys. Lett. B* 749 (2015) 262
- [150] Yan Zhang *et al.*, *Phys. Rev. C* 95 (2017) 041602(R)
- [151] A.B. McIntosh, S.J. Yennello, *Progress in Particle and Nuclear Physics* 108 (2019) 103707
- [152] K.Stiefel *et al.*, *Phys. Rev. C* 90 (2014) 061605(R)
- [153] S. Valdré *et al.*, *Nucl. Instr. and Meth. A* 930 (2019) 27
- [154] P. Danielewicz, *Nucl. Phys. A* 673 (2000) 375
- [155] A. Andronic, J. Lukasik, W. Reisdorf and W. Trautmann, Systematics of stopping and flow in Au+Au collisions, *Eur. Phys. Jou.A* 30 (2006) 31 , Società Italiana di Fisica / Springer-Verlag 2006
- [156] A. Andronic *et al.*, *Phys. Lett. B* 612 (2005) 173
- [157] C. Pinkenburget *et al.*, *Phys. Rev. Lett.* 83 (1999) 1295
- [158] P. Braun-Munzinger, J. Stachel, *Nucl. Phys. A* 638 (1998) 3c
- [159] B.A. Li, B. Das Champak, S. Das Gupta and C. Gale, *Nucl. Phys. A* 735 (2004) 563
- [160] J. Rizzo, M. Colonna and M. Di Toro, *Phys. Rev. C* 72 (2005) 064609
- [161] Bao-An Li, Bao-Jun Cai, Lie-Wen Chen *et al.*, *Progress in Particle and Nuclear Physics* 99 (2018)

- [162] B-A Li *et al.*, *Phys. Rev. Lett.* 88 (2002) 192701
- [163] P. Russotto *et al.*, *Phys. Lett. B* 697 (2011) 471
- [164] M.D. Cozma, *Phys. Lett. B* 700 (2011) 139
- [165] V. Giordano *et al.*, *Phys. Rev. C* 81 (2010) 044611
- [166] M.D. Cozma *et al.*, *Phys. Rev. C* 88 (2013) 044912
- [167] P. Danielewicz and J. Lee, *Nucl. Phys. A* 922 (2014) 1
- [168] B. A. Brown, *Phys. Rev. Lett.* 111 (2013) 232502
- [169] Z. Zhang and L. W. Chen, *Phys. Lett. B* 726 (2013) 234
- [170] C.Fuchs, A.Faessler, E.Zabrodin, Y.-M.Zheng, Probing the nuclear equation of state by K+ production in heavy-ion collisions, *Phys. Rev. Lett.* 86 (2001) 1974
- [171] G.Ferini *et al.*, *Phys. Rev. Lett.* 97 (2006) 202301
- [172] M.D. Cozma, *Phys. Lett. B* 753 (2016) 166
- [173] T. Song, C.M. Ko, *Phys. Rev. C* 91 (2015) 014901
- [174] Bao-An Li, *Phys. Rev. C* 67 (2003) 017601
- [175] G. Ferini, M.Colonna, T.Gaitanos, M.Di Toro, *Nucl. Phys. A* 762 (2005) 147
- [176] W.Reisdorf *et al.*, FOPI Collaboration, *Nucl. Phys. A* 781 (2007) 459
- [177] J. Hong and P. Danielewicz, *Phys. Rev. C* 90 (2014) 024605
- [178] C. Guo *et al.*, *Phys. Rev. C* 91 (2015) 054615
- [179] Z. Feng, *Eur.Phys.Jou. A* 53 (2017) 30
- [180] Z. Zhang and C-M Ko, *Phys. Rev. C* 95 (2017) 064604
- [181] M.D. Cozma *et al.*, *Phys. Rev. C* 95 (2017) 014601
- [182] N. Ikeno *et al.*, *Phys. Rev. C* 93 (2016) 044612 ; N. Ikeno, A. Ono, Y. Nara, A. Ohnishi, Erratum: Probing neutron-proton dynamics by pions[*Phys. Rev. C* 93, 044612 (2016)], *Phys. Rev. C* 97 (2018) 069902(E)
- [183] M.B. Tsang *et al.*, *Phys. Rev. C* 95 (2017) 044614
- [184] J.Xu *et al.*, *Phys. Rev. C* 93 (2016) 044609
- [185] Y.Zhang *et al.*, *Phys. Rev. C* 97 (2018) 034625
- [186] A.Ono *et al.*, *Phys. Rev. C* 100 (2019) 044617
- [187] P.Morfouace *et al.*, *Phys. Lett. B* 799 (2019) 135045